UNIVERSITY OF CALIFORNIA, SAN DIEGO

Manipulation of Delicate Objects in Robotics and Medicine: A Design Approach

A Thesis submitted in partial satisfaction of the
requirements for the degree
Master of Science

in

Engineering Science (Mechanical Engineering)

by

Tom Kalisky

Committee in charge:

Professor Michael T. Tolley, Chair
Professor Eliah Aronoff-Spencer, Co-Chair
Professor Nick Gravish

2017

The thesis of Tom Kalisky is approved, and it is acceptable in quality and form for publication on microfilm and electronically:

Co-Chair

Chair

University of California, San Diego

2017

EPIGRAPH

To the optimist, the glass is half full.

To the pessimist, the glass is half empty.

To the engineer, the glass is twice as big as it needs to be.

—Anonymous

TABLE OF CONTENTS

Signature Page . . . iii

Epigraph . . . iv

Table of Contents . . . v

List of Figures . . . vii

List of Tables . . . ix

Acknowledgements . . . x

Vita . . . xi

Abstract of the Thesis . . . xii

Chapter 1 Introduction . . . 1
- 1.1 Background . . . 1
- 1.2 Layout . . . 2

Chapter 2 Differential Pressure Control of 3D Printed Soft Fluidic Actuators 3
- 2.1 INTRODUCTION . . . 4
  - 2.1.1 Background . . . 4
  - 2.1.2 3D Printed Soft Actuator . . . 6
  - 2.1.3 Contributions and Layout . . . 7
- 2.2 Volumetric Control System Design . . . 9
- 2.3 Experimental Characterization . . . 10
  - 2.3.1 Working Pressure Limits . . . 12
  - 2.3.2 Blocked Force Comparison . . . 13
  - 2.3.3 Actuator Workspace Comparison . . . 14
  - 2.3.4 Operation of Ruptured Actuators with Negative Pressure Actuation . . . 18
  - 2.3.5 Hand Writing Demonstration . . . 19
  - 2.3.6 Suction Cup Manipulation Demonstration . . . 20
- 2.4 Finite Element Analysis of Differential Pressure Actuation . 22
- 2.5 CONCLUSIONS . . . 23

Chapter 3 Human Centered Design for Biometric Identification of Infant for Vaccinations . . . 25
- 3.1 Introduction . . . 26
- 3.2 Methods / Approach . . . 30
  - 3.2.1 Testing of Existing Technology . . . 30

3.2.2 Design Evolution Approach Taxonomy 31
3.2.3 Study Approach 35
3.2.4 Image Processing Approach 35
3.2.5 Fingerprint Quality Evaluation 39
3.3 Results 41
3.3.1 Understating Failure Modes 41
3.3.2 Data Analysis 48
3.4 Discussion 51
3.5 Conclusion 53
3.6 Future Work 53

Appendix A Starfish 56

Appendix B Laser Drawing Code 58

Appendix C A Detailed Biometrics Table 71

Appendix D Hardware Modules and Caps 74

Bibliography 76

LIST OF FIGURES

Figure 2.1: Closed system for differential pressure actuation and control of 3D printed soft fluidic actuators. a) Demonstration of actuation and manipulation of a delicate object. b) Volumetric control system for positive and negative, pneumatic or hydraulic actuation of soft robotics. 5

Figure 2.2: Volumetric Control System Design: a) Rendered image of the system with main components annotated. b) Schematic drawing of the system illustrating the interconnections of the components. c) A single syringe pump module detached from the main system. d) . . 8

Figure 2.3: 3D Printed Soft Actuator: a) Actuation of different chambers of the actuator. b) Radial plane cross section of a single chamber. c) Transverse plane cross-section of the actuator. 11

Figure 2.4: a) Experimental test setup [1, 2] used to measure actuator force output. b) Tip force for different actuation modes (error bars represent standard deviation) Pressure test was performed at 60 kPa. Vacuum test was performed at -95 kPa gauge. Differential testing was . . . 14

Figure 2.5: Bending angle comparison measured from non-actuated position. a) Bending using only vacuum at -95 kPa. b) Bending using only pressure at 60 kPa. c) Differential pressure bending using combination of pressure at 60 kPa in two chambers and vacuum at -69 kPa . . . 16

Figure 2.6: Actuator linear displacement. a) Three chambers inflated to 69 kPa. b) Three chambers at 0 kPa. c) Three chambers at -60 kPa. 17

Figure 2.7: a) A rupture created on the actuator due to delamination of the 3D printed layers. b) Actuator's bend angle comparison for different actuation with ruptured and intact actuators (error bars represent standard deviation) 18

Figure 2.8: Hand Writing Demonstration Setup. I manipulated the actuator with a laser pointer at the tip of it in the axial direction and a web-cam (not displayed) was used to track the laser light 21

Figure 2.9: Bending angle comparison for experimental and the finite element model with 60 kPa in a single chamber and -30 kPa in the other two chambers. a) Experimental results bending angle of 79 degrees. b) Simulation results bending angle of 58 degrees. c) Comparison) . . 23

Figure 3.1: Design Evolution Approach Taxonomy; This figure illustrates the two approaches we took for fingerprint imaging. To the right is contact methods where the fingerprint area on the skin comes in contact with an imaging surface. The left branching path is 32

Figure 3.2: Fingerprint processing pipeline; a) Processing from raw image, to binarized image.b) Reliability Matrix. c) Coherence and corruption maps. d) Raw contact fingerprint. e) Raw non-contact fingerprint . 36

Figure 3.3: Fishbone diagram of causes to poor quality. Four main groups which incorporate features that lead to fingerprint failure. The four groups (a-d) correlate to the four sub-figures in [Fig. 3.4] 45
Figure 3.4: Example of failures in print capture; a) Examples of finger characterstics that cause poor printb)Interaction failures c) Imager system failures. d) Illumination failure modes 46
Figure 3.5: Two samples for high quality fingerprints: a) Contact fingerprint, b) Non-contact fingerprint 47
Figure 3.6: A bar graph of the accepted contact prints (blue) vs. the rejected prints (yellow) 49
Figure 3.7: A bar graph of the accepted non-contact prints (blue) vs. the rejected prints (yellow) 49
Figure 3.8: A bar graph of the matched contact prints (blue) vs. the rejected prints (yellow) 50
Figure 3.9: A bar graph of the matched non-contact prints (blue) vs. the rejected prints (yellow) 51
Figure 3.10: Contact (red) and non-contact (blue) fingerprint matching accuracy vs 1:N matching result from the three infants. Where is number of individual fingers. 52
Figure 3.11: Matching accuracy vs. subject's age where the blue plot is for contact imaging and red is for non-contact. 52
Figure 3.12: Process of making a lifelike replica of an infant's hand with accurate fingerprint features. a) A silicone mold of a 7 year old. b) Same hand as in 'a' which was cast in Hydrospan and left to shrink. c) the shrunken hand model cast in silicone. 54

Figure A.1: a) A diagram showing a cut view of the locomotion of the starfish through contraction and relaxation of the muscle. b) A rendering of the proposed actuator with hydraulic chambers inside the outer walls which simulate the contracting muscles of the biological counter . . 57

Figure C.1: Part A of a detailed table comparing the different characteristics of biometrics identifiers to assist in selecting the most appropriate identifier for each identification requirement. 72
Figure C.2: Part B of a detailed table comparing the different characteristics of biometrics identifiers to assist in selecting the most appropriate identifier for each identification requirement. 73

Figure D.1: Computer Aided Design (CAD) line drawing of the final hardware modules and interaction caps that fit on top of this modules. 75

LIST OF TABLES

Table 2.1: Bill of Materials 10
Table 2.2: Working Pressure Limits 13

Table 3.1: Biometrics Traits 28

ACKNOWLEDGEMENTS

- Thanks to My Committee:
  - **Michael T. Tolley** for the direction, instructions, and countless paper edits.
  - **Eliah Aronoff-Spencer** for the opportunity, support and counseling.
  - **Nicholas Gravish** for advising, and the helpful opinion.
- **The KidPrint team** for all their hard work, help and contribution to my thesis, mainly **Deborah Forster** for the guidance and mentoring.
- **The Bio-Inspired Robotics and Design Lab group** for the assistance, collaboration and comradery.

Chapter 2, in full, has been submitted for publication of the material as it may appear in (2017) ”Differential Pressure Control of 3D Printed Soft Fluidic Actuators”, Int. Conf. on Intelligent Robots and Systems (IROS), Vancouver, Sept. 2017. Kalisky T., Wang Y., Shih B., Drotman D., Jadhav S., Aronoff-Spencer E., and Tolley M T. The dissertation/thesis author was the primary investigator and author of this paper.

Chapter 3, in part is currently being prepared for submission for publication of the material. Kalisky; Tom; Forster, Deborah; Tolley, Michael T; Aronoff-Spencer Elaih. The dissertation/thesis author was the primary investigator and author of this material.

VITA

2015	B. S. in Mechanical Engineering Technology *summa cum laude*, University of North Texas
2015-2017	Graduate Research Assistant, University of California, San Diego
2017	MS. in Mechanical Engineering, University of California, San Diego

PUBLICATIONS

Tom Kalisky, "Differential Pressure Control of 3D Printed Soft Fluidic Actuators", *Int. Conf. on Intelligent Robots and Systems (IROS)*, 2017.

ABSTRACT OF THE THESIS

Manipulation of Delicate Objects in Robotics and Medicine: A Design Approach

by

Tom Kalisky

Master of Science in Engineering Science (Mechanical Engineering)

University of California, San Diego, 2017

Professor Michael T. Tolley, Chair
Professor Eliah Aronoff-Spencer, Co-Chair

In this work, I explore two facets of manipulation of delicate objects. First I describe the development of a new closed system for differential pressure control of 3D printed soft fluidic actuators. I further explore the quantitative advancements it promises for soft robotics towards a robotics manipulator capable of safely and efficiently manipulating infants fingers. Secondly, we present the development of a biometrics system for vaccinations which requires manipulation and imaging of infants fingers. The fingerprinting process could highly benefit from automation solutions for infants fingerprint platen induced deformation due to contact. The next aspect of my thesis is

the experimental approach for iterative testing in technology design. Starting with the volumetric control platform developed to enable accurate iterative testing in laboratory settings for experimental characterization of soft actuators with differential pressure control. In this work, I demonstrated a substantial improvement in achievable blocked force, and a significant increase in actuator workspace when using differential pressure actuation as compared to the use of only pressure or vacuum. The increased workspace allowed the robot to achieve complex tasks towards manipulation of fragile objects. Furthermore, I demonstrate a self-healing capability of the combined system for improved soft robotics robustness. Then I follow with an approach for human-centered design with iterative prototyping where experiments can only be performed in situ with live infant subjects. This separation between the design and experiments yields a very challenging progress evaluation and required a unique design iteration methodology. With the resulted fingerprints images from the two leading devices, I demonstrated a higher reliability for high quality infants fingerprints using non-contact imaging over contact in the goal of developing a reliable biometrics identification system of infants for vaccination.

Chapter 1

Introduction

1.1 Background

Manipulation of delicate objects has many applications as an assistive agent in the home [3], in medicine [4, 5], and is a very promising aspect of robotics [6, 7]. However, there are still challenges to incorporating robots into the home for physical human-robot interaction. Soft robotics is an encouraging class of robotics for safer operation near people and for interaction with humans thanks to their compliant nature and the ability to absorb energy from impact without damage [8]. These qualities make soft robots favorable over rigid-bodied robots for interaction with humans [9], handling of delicate and fragile objects [10, 11] and operations that challenge human skilled performance [12, 13].

Fingerprinting is an extensively studied approach for biometric identification systems and is commonly used in many different industries from criminal justice and security to healthcare. Previous attempts were made to adapt adult fingerprinting systems for infants with very limited success. The infant fingerprinting process requires the positioning of the infant's finger in a specific position with a very precise and delicate action since any contact with the fingerprint area can cause deformation to the print. Therefore, manipulation tasks such as holding an infant's finger could highly benefit from a soft robotic manipulator precise enough and is capable of varying its stiffness to manipulate and hold an infant's finger in place while being compliant enough to not harm the infant.

1.2 Layout

In this work, I explore two aspects of manipulation of delicate objects. In chapter 2, I begin by describing a new volumetric control system for actuation of soft fluidic actuators and studying the advantages of combining vacuum and pressure modes for 3D printed fluidic actuators. The chapter then provides an overview of the design of the volumetric control system. Followed by section (Section 2.3) which then discusses the experimental characterization of the 3D printed actuators with actuation using differential pressure control. In section 2.4, I describe the finite element model of the 3D printed actuator and present a simulation of the differential pressure actuation. Finally, section 2.5 provides a conclusion and a brief discussion of future work. Chapter 3 then begins with a background on vaccination efforts and continuous with literature review of biometric identification for infants and young children. Section 3.2 describes our approach for design iteration and experimental testing for this study. Then section 3.3 shows the results, first for the different failure modes and then for image processing and matching. Lastly, the chapter concludes with a discussion of the results, conclusions, and additional future work.

Chapter 2

Differential Pressure Control of 3D Printed Soft Fluidic Actuators

Fluidically actuated soft robots show a great promise for operation in sensitive and unknown environments due to their intrinsic compliance. However, most previous designs use either flow control systems that are noisy, inefficient, sensitive to leaks, and cannot achieve differential pressure (i.e. can only apply either positive or negative pressures with respect to atmospheric), or closed volume control systems that are not adaptable and prohibitively expensive. In this chapter, I present a modular, low cost volume control system for differential pressure control of soft actuators. I use this system to actuate three-chamber 3D printed soft robotic modules. For this design, I find a 54% increase in achievable blocked force, and a significant increase in actuator workspace when using differential pressure actuation as compared to the use of only pressure or vacuum. The increased workspace allowed the robot to achieve complex tasks such as writing on a screen with a laser pointer or manipulating fragile objects. Furthermore, I demonstrate a self-healing capability of the combined system by using vacuum to actuate ruptured modules which were no longer responsive to positive pressure.

2.1 INTRODUCTION

2.1.1 Background

Drawing inspiration from nature [Appendix A], the high compliance of soft robots results in advantageous features including large active and passive continuous deformations, and the ability to absorb energy from impact without damage [8]. These qualities make soft robots favorable over rigid-bodied robots for interaction with humans [9], handling of delicate and fragile objects [10, 11], and for maneuvering in unknown and variable, or sensitive environments [14, 15, 16]. Based on this promise, recent work has proposed to use soft robotics for medical devices for minimally invasive surgery [17], and diagnosis [18], and safe robotic assisted home care[19].

Despite their advantageous capabilities, and in fact due to the same qualities, general approaches to control and actuation of soft robots are open challenges[8, 20]. The compliant nature of soft robots requires a different control system than a conventional hard-body robot and makes the task of driving such robots challenging. Several methods have been proposed for the actuation of soft robots; one commonly used approach is shape memory wires which deform to a desired shape when heated [21]. Another emerging approach is electroactive polymers which are adopted for actuators and sensors as they change shape and size when exposed to an electric field, and vice versa [22]. Actuating a soft robot by pulling on properly positioned tensile cables that act like biological tendons is another technique that takes advantage of the high tensile loading capabilities of cables while still being sufficiently compliant to prevent any bending or compression constraints on the soft body [11]. Fluidic Elastomer actuators (FEAs) [20, 23, 24, 25] take advantage of the ability of a pressurized fluid to adjust itself to apply even pressure on a containing boundary to maintain an adaptive yet consistent mechanism for soft robotics. Most

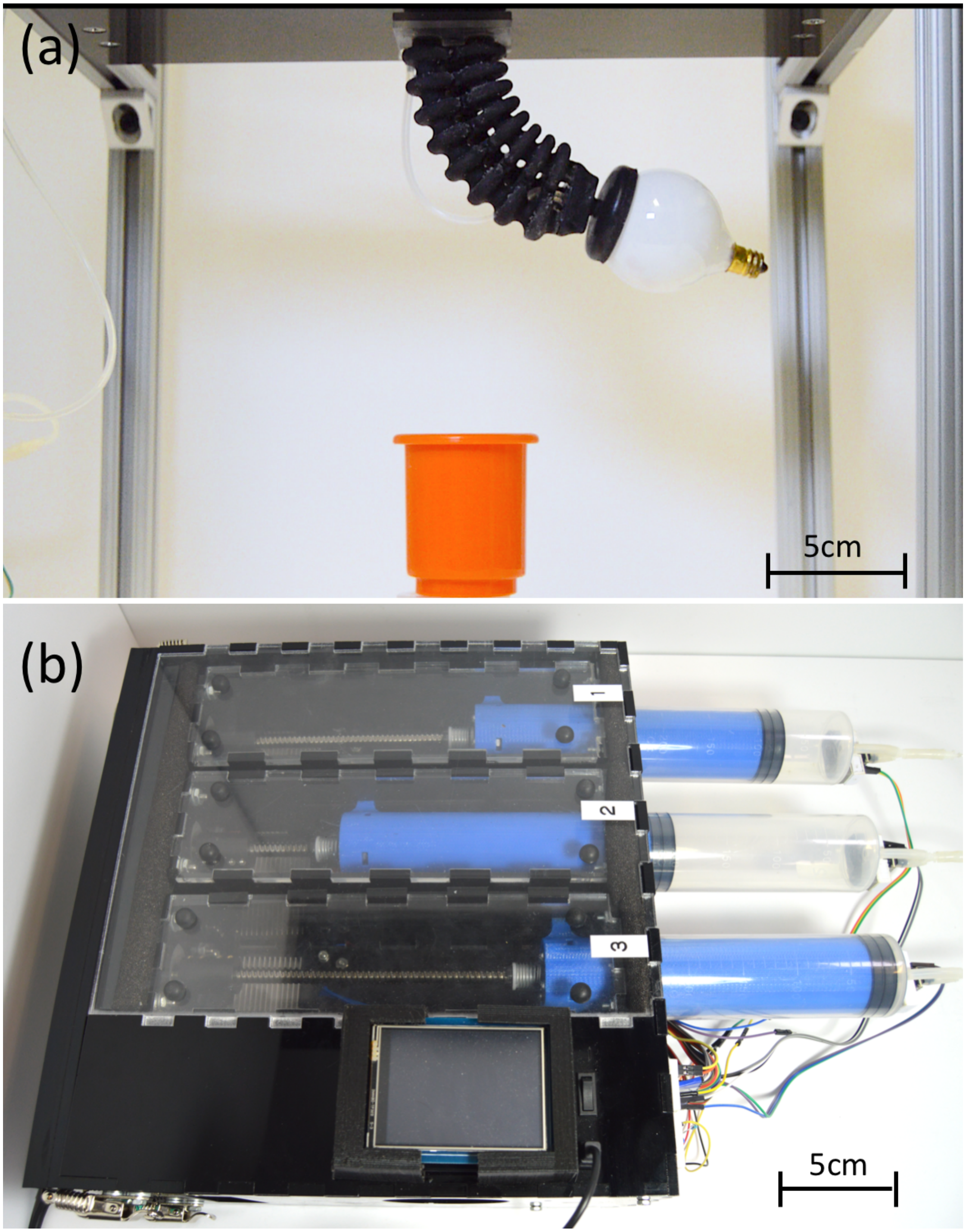

Figure 2.1: Closed system for differential pressure actuation and control of 3D printed soft fluidic actuators. a) Demonstration of actuation and manipulation of a delicate object. b) Volumetric control system for positive and negative, pneumatic or hydraulic actuation of soft robotics.

soft robots powered by either pneumatics [23] or hydraulics [26] employ a pump and a system of valves that control internal fluid flow to inflate and deflate their actuators [23]. These open (pump and valves) systems frequently use the pulse-width modulation (PWM) to switch on the solenoid valves for pressure control. Although very simple and relatively easy to implement, the open systems are noisy and inefficient. Therefore, other methods have been developed which use a closed system control with a cylinder-piston design which allows for a more precise volume regulation while coupling each cylinder with an actuated segment [27, 28]. This coupling eliminates the exhaust of pressurized air to the environment, reducing a key source of energy loss, resulting in increased efficiency and reduced noise. Furthermore, a high gear reduction between motor and piston allows the soft modules to hold position with minimal actuator effort. Although they are very efficient, commercially available syringe pumps are not only expensive but typically designed for small volumes and flow rates [29] A previously developed volume control systems for soft robots likewise employ expensive components [10]. Furthermore, previous systems have not demonstrated simultaneous pressure and vacuum operation, or the ability to use a variety of working fluids for soft robotics.

2.1.2 3D Printed Soft Actuator

Soft actuators pose many challenges not only in control but also in design and fabrication [30]. Commonly used fabrication techniques for FEAs actuators such as soft lithography [31, 32] require many steps and are either limited to the fabrication of 2.5 D structures or require complex 3D molding techniques. To avoid these laborious fabrication processes, I, and other soft roboticists have adapted the use of 3D printers for the task [33, 34, 35, 1]. The high resolution and the capability of printing multiple materials in a single part enable the facile, rapid fabrication of complex actuator designs. Despite the advantages of 3D printing, challenges in the design of actuators remain due to uncertainty in the materials deposition pattern making the characterization of 3D printed soft actuators very challenging, and the materials themselves are often proprietary or poorly characterized. To test our hypothesis for the functionality of the system and improved performance of 3D printed soft fluidic actuators I used a modular actuator design incorporating three parallel, externally connected chambers rotated 120 degrees about the longitudinal axis of the actuator [23]. In previous work, I proposed a 3D printed bellowed version of this design (Fig. 2.3) [1]. The actuator was fabricated using a multi-material 3D printer (Objet 350 Connex 3, Stratasys) printed from a rubber-like material (FLX9070-DM), a mixture of a rigid (Veroclear) and a soft material (TengoBlackPlus). By varying the internal pressure within each chamber, the actuator can elongate, compress, and bend in any radial direction. The bellow design folds and unfolds during actuation reducing the tensile stress in the material as compared to comparable straight-tube elastomeric design [36].

2.1.3 Contributions and Layout

In this chapter, I describe a new volumetric control system for actuation of soft fluidic actuators and study the advantages of combining vacuum and pressure modes for 3D printed fluidic actuators. The contributions of this chapter are:

- The design of a low-cost system for volumetric pneumatic and hydraulic control of soft fluidic actuators.
- The description of an approach to employ the simultaneous vacuum and pressure (i.e. differential pressure) actuation for closed loop control of pneumatically actuated soft robots.
- Demonstration of improved performance of 3D printed soft fluidic actuators in terms of workspace, bend-angle, tip forces and robustness under combination of

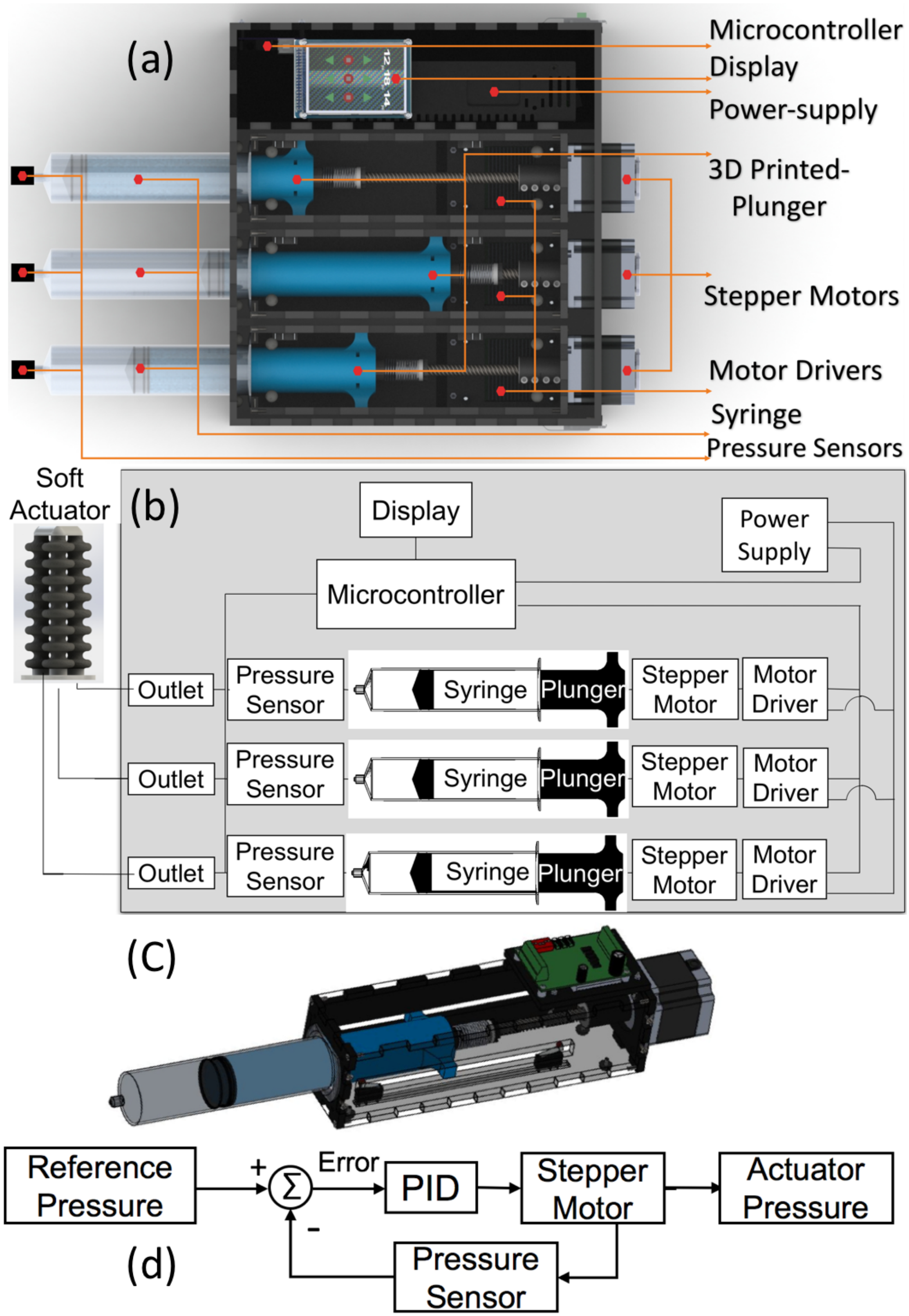

Figure 2.2: Volumetric Control System Design: a) Rendered image of the system with main components annotated. b) Schematic drawing of the system illustrating the interconnections of the components. c) A single syringe pump module detached from the main system. d) Block diagram of the PID control loop implemented in each module

vacuum and pressure actuation.

In the next section (Section II) I present an overview of the design of the volumetric control system. The following section (Section III) discusses the experimental characterization of the 3D printed actuators with actuation using differential pressure control. In section IV, I describe the finite element model of the 3D printed actuator and present a simulation of the differential pressure actuation. Finally, section V provides a conclusion and a brief discussion of future work.

2.2 Volumetric Control System Design

For the purpose of actuating a large variety of soft fluidic actuators, (including the 3D printed soft actuators discussed above) I developed a modular volumetric control system (Fig.2.2). The system consists of interchangeable cylinder pump units that can be replaced if necessary or added depending on the application. Each unit is capable of inflating and deflating a chamber within a soft actuator by displacing fluidic volume.

The control system is composed of modular piston units. I chose to use commercially available plastic syringes to allow for adjustability in the displacement volume and type of actuation fluids while maintaining affordability and replaceability. I tested both 140cc and 200cc syringes, and used the latter for the experiments described in this paper. I replaced the plunger of each syringe with a 3D printed part with a center hole to accommodate a threaded rod. I used the rubber cap from the original syringe plunger on the 3D printed replacement to maintain the correct fit and prevent leaks. Each unit contains a stepper motor (Nema 23 CNC Stepper Motor 2.8A 178.5oz.in/1.26Nm), driven by a stepper motor driver (Uxcell TB6560 3A Single-Axis Stepper Motor Driver Board). Each motor rotates a threaded rod that drives a nutattached to the 3D printed plunger. As a result, rotational motion of the stepper motor is converted to linear motion of the plunger. The system is powered by a 360 W, 24 V power supply, controlled with a microcontroller (Arduino Mega 2560), and uses a display screen for visual interface. Each syringe outlet is mounted with a pressure sensor (SSCDANT150PGAA3 Honeywell Pressure Sensor) for pressure feedback. Table I lists the costs of components which form the volumetric control system.

Table 2.1: Bill of Materials

Component	Quantity	cost per item	Total cost
200cc Plastic Syringe	3	$17	$51
Nema 23 Stepper Motor	3	$26	$78
Stepper Motor Driver	3	$10	$30
Threaded Rod 3’	1	$8	$8
Leadnut and Coupler	3	$35	$105
Power Supply	1	$23	$23
Microcontroller	1	$35	$35
Display	1	$28	$28
Pressure Sensor	3	$41	$123
Total			$481

I implemented a closed-loop PID controller with actuator pressure feedback for error calculation. The block diagram of the control loop can be seen in (Fig. 2.2(d)).

2.3 Experimental Characterization

I chose a set of experiments to evaluate performance metrics to compare the operation of the volumetric control system based on actuator capabilities. G. Agarwal et al. [37] presented a criterion for evaluation of new soft actuators. This criterion uses the performance requirements of force output and required displacement which are needed to complete an action to gauge actuator’s behavior and to design durable and effective actuators. I compared the actuators performance between the three different actuation

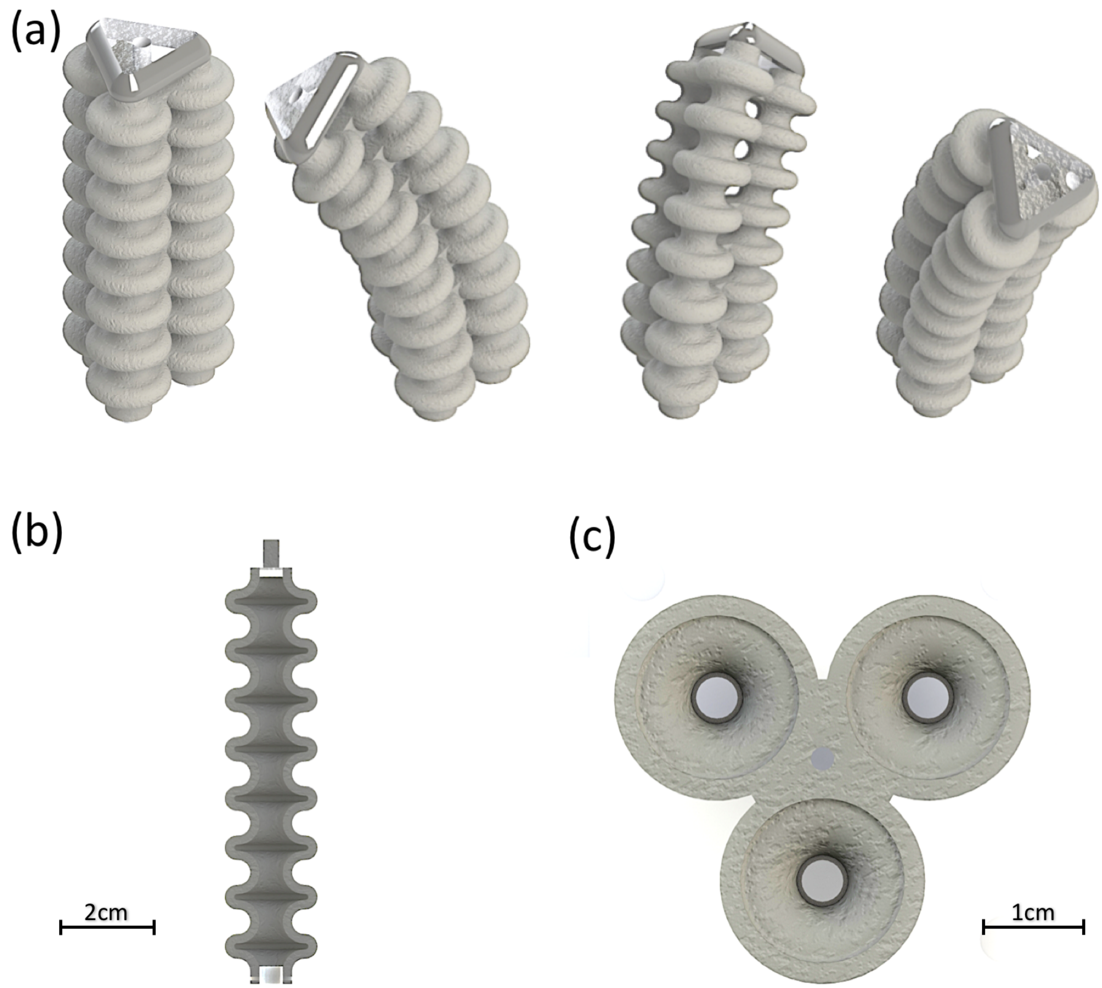

Figure 2.3: 3D Printed Soft Actuator: a) Actuation of different chambers of the actuator. b) Radial plane cross section of a single chamber. c) Transverse plane cross-section of the actuator.

modes: inflation or positive pressure, deflation or negative pressure and the combination of both applied to separate chambers in a single actuator. For the rest of this paper I will refer to pressure values relative to atmospheric pressure with positive pressure for gauge pressure and negative pressure for vacuum.

2.3.1 Working Pressure Limits

To get an accurate comparison between the different actuation modes and to characterize the limits of safe operation in term of output angles and forces, I first determined the failure point in each mode. The failure point is the actuation state at which the stresses generated by the pressure of the working fluid inside the chambers, relative to the external atmospheric pressure caused a rupture in the actuator wall. In this experiment, I first tested for failure points by applying pressure only to a single chamber, starting from 0 kPa and increasing by increments of 1.72 kPa (.25 psi) every ten seconds until rupture was observed. A delay of ten seconds between each increment was necessary to allow for the viscoelastic material to relax completely. For the vacuum failure point, I repeated the same experiment except with decreasing pressure, down to the maximum negative pressure achievable by the volumetric control system (-95 kPa gauge). To find the failure point for combinations of vacuum and pressures, I first applied a constant negative pressure -69 kPa gauge to a single chamber. This value was selected for practical reasons (Although the system is capable of applying up to -95 kPa for the tested actuator, the operation of vacuuming brings the plunger close to its movement limit and does not leave enough space for control adjustments.) After vacuum was applied to a single chamber, the two adjacent chambers were inflated in increments of 1.72 kPa every ten seconds until one of the two inflated actuated chambers was ruptured.

I used these experimental results to set the limit pressures (see Table II) to prevent actuator damage in subsequent experiments. When actuating using only positive pressure, the actuators failed at an average pressure of 105 kPa. Our testing show that at the highest vacuum our system is capable of producing (-95 kPa) the actuators did not show any sign of failure. For the differential test, the pressurized chambers failed at an average pressure of 64 kPa. Based on these results I set the global limit for the actuators working pressure to 60 kPa.

Table 2.2: Working Pressure Limits

Actuation Mode	Pressure	Vacuum	Differential
Average Failure Point (kPa)	105	N/A	64
Standard Deviation	0.25	N/A	1.44

2.3.2 Blocked Force Comparison

Blocked force (the force applied by an actuator when the tip displacement is constrained to be zero) is a critical parameter for characterizing an actuators capabilities. To compare how the three different modes of pressurization affect the performance of this actuator, I used an experimental test setup (Fig. 2.4) [2]] that measures the force applied by the bending actuator. The test setup is made up of a single axis load cell (FX1901, Measurement Specialties) mounted to test vertical force, a microcontroller (Ardunio Uno) used to collect data from the load cell, a stepper motor (NEMA 17, Adafruit), and a stepper driver (Easy Driver, Sparkfun) to align the actuator with the load cell. The actuator was mounted horizontally with the tip aligned with the load cell, to measure the perpendicular force applied by the tip of the actuator. I tested the actuator with a negative pressure of -95 kPa applied to a single chamber, a positive pressure of 60 kPa applied to a single chamber, and a combination of -69 kPa two chambers and 60 kPa in the third chamber (all oriented to apply a downward force at the tip). The experiment was repeated four times for each actuation mode and the data was recorded for each

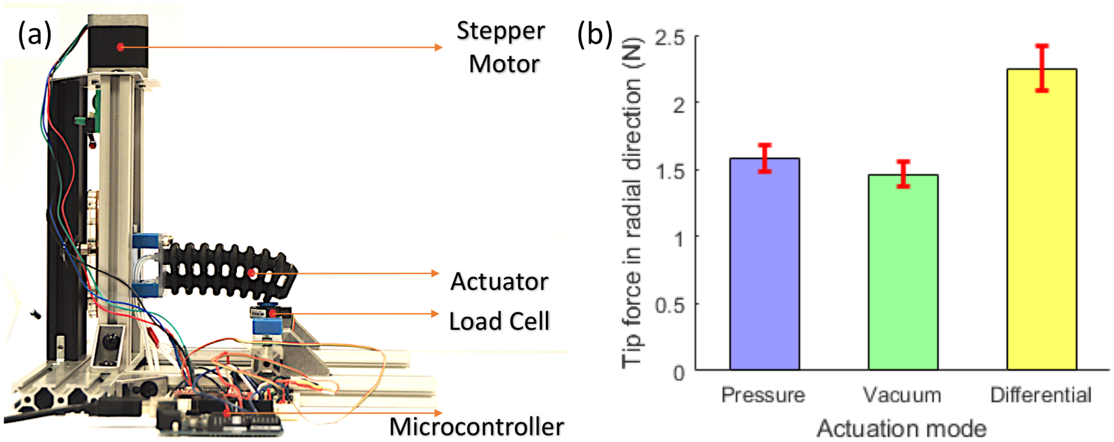

Figure 2.4: a) Experimental test setup [1, 2] used to measure actuator force output. b) Tip force for different actuation modes (error bars represent standard deviation) Pressure test was performed at 60 kPa. Vacuum test was performed at -95 kPa gauge. Differential testing was performed with 60 kPa pressure and 69 kPa vacuum

trial. A comparison of the blocked force results in (Fig. 2.4) shows that a tip output force in the radial direction using positive pressure produced 1.57 N on average (this is consistent with our previous measurements for this case which averages 1.5 N [24]). The use of negative pressure similarly resulted in an average of 1.45 N force. However, the combination of vacuum and pressure resulted in an average of 2.25 N force, an improvement of 54% and 43% over actuation using only negative or positive pressure (respectively).

2.3.3 Actuator Workspace Comparison

The no-load displacement of the actuator was the second performance measure I used to compare the different actuation modes.I first measured the displacement in terms of bend angle of the module and secondly in terms of the elongation of the module. To evaluate the bend angle, I placed the actuator vertically and attached a needle to the actuator tip in the axial direction and measured the angle between the position of the needle before actuation and at the maximum deflection (Fig. 2.5). I repeated this experiment four times for each of the three actuation modes with pressure limits set by practical system limitations as discussed above (i.e. vacuum at -95 kPa, pressure at 60 kPa, and finally combination of negative pressure at -69 kPa with a positive pressure of 60 kPa for two actuators in vacuum and one in pressure and then for two actuators in pressure and one in vacuum).

The results of the differential test show an increase of 101% in the bend angle with respect to the positive pressure test and a 98% increase with respect to the negative pressure test. A polar plot of these results in (Fig. 2.5d) demonstrates the achievable bending angle in each spatial direction of the actuators for the different actuation modes. Note that only a third of the workspace is unique due to symmetry. For six of these points, the chambers are actuated at the positive and negative pressure limits listed in Table 1. For the six intermediate points, I determined the relative pressure values using the following relationship[23]

$$\tan(\theta) = \frac{(2P1 - P2 - P3)}{(\sqrt{3}(P2 - P3))} \tag{1}$$

where Pi is the pressure in chamber i and θ is the azimuth angle of the bent actuator. This plot highlights the effective increase in the achievable workspace due to differential pressure. Three parameters: bend angle, azimuth angle, and elongation fully define the configuration of the actuator. Differential pressure control not only enables a higher bend angle but is also required to independently control these three degrees of freedom.

For the elongation test I evaluated the maximum linear displacement that can be achieved using differential pressure control for the soft actuator (Fig. 2.6). The maximum elongation with 60 kPa pressure in all three chambers was 15.6mm while the maximum shortening by applying -69 kPa in all three chambers was 21 mm. Overall the actuator underwent 37% axial deformation from minimum length to maximum length.

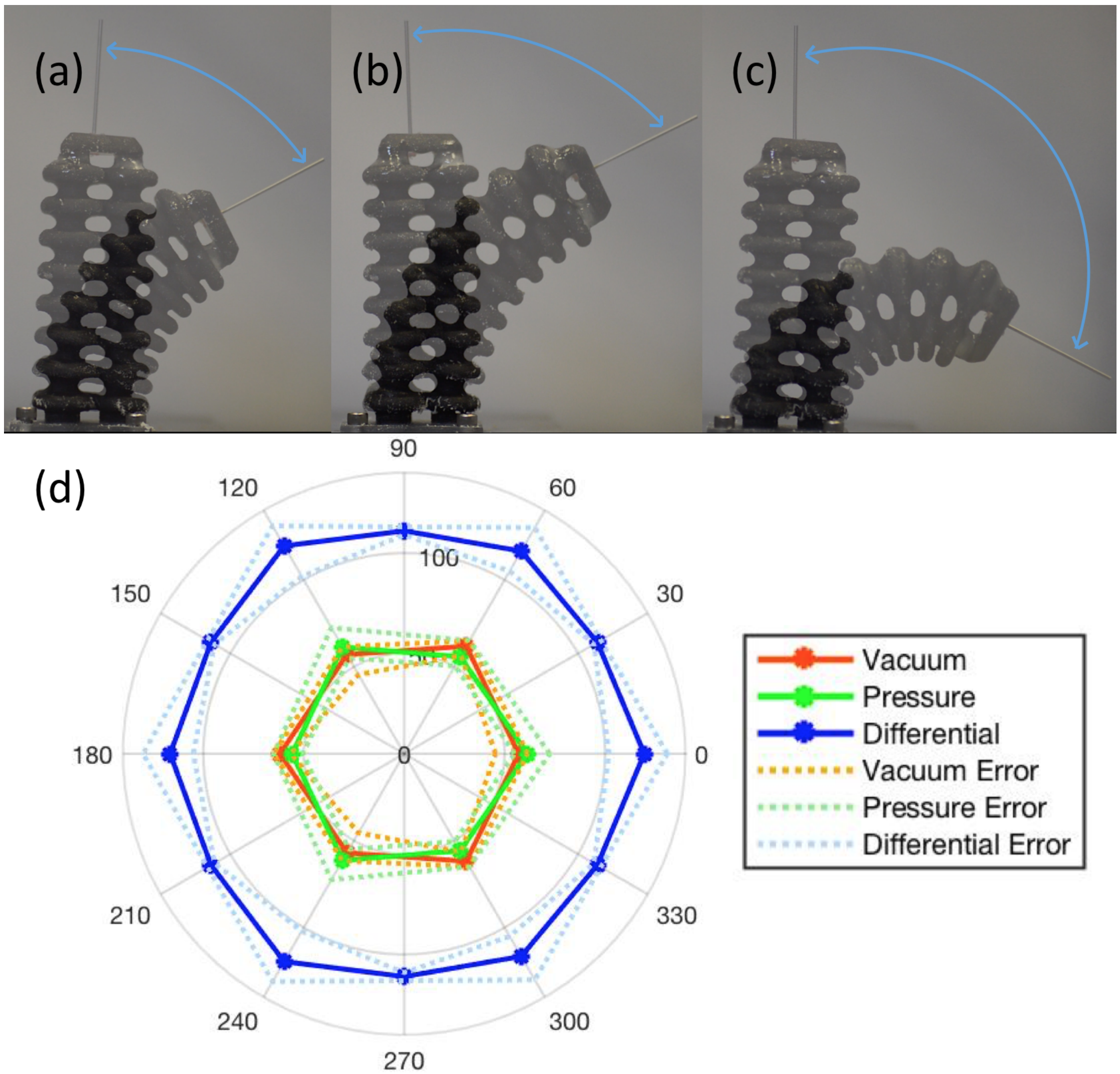

Figure 2.5: Bending angle comparison measured from non-actuated position. a) Bending using only vacuum at -95 kPa. b) Bending using only pressure at 60 kPa. c) Differential pressure bending using combination of pressure at 60 kPa in two chambers and vacuum at -69 kPa in the third chamber. d) The average bending angle for each mode of actuation for 12 azimuth angles showing the increase in the actuator's work space

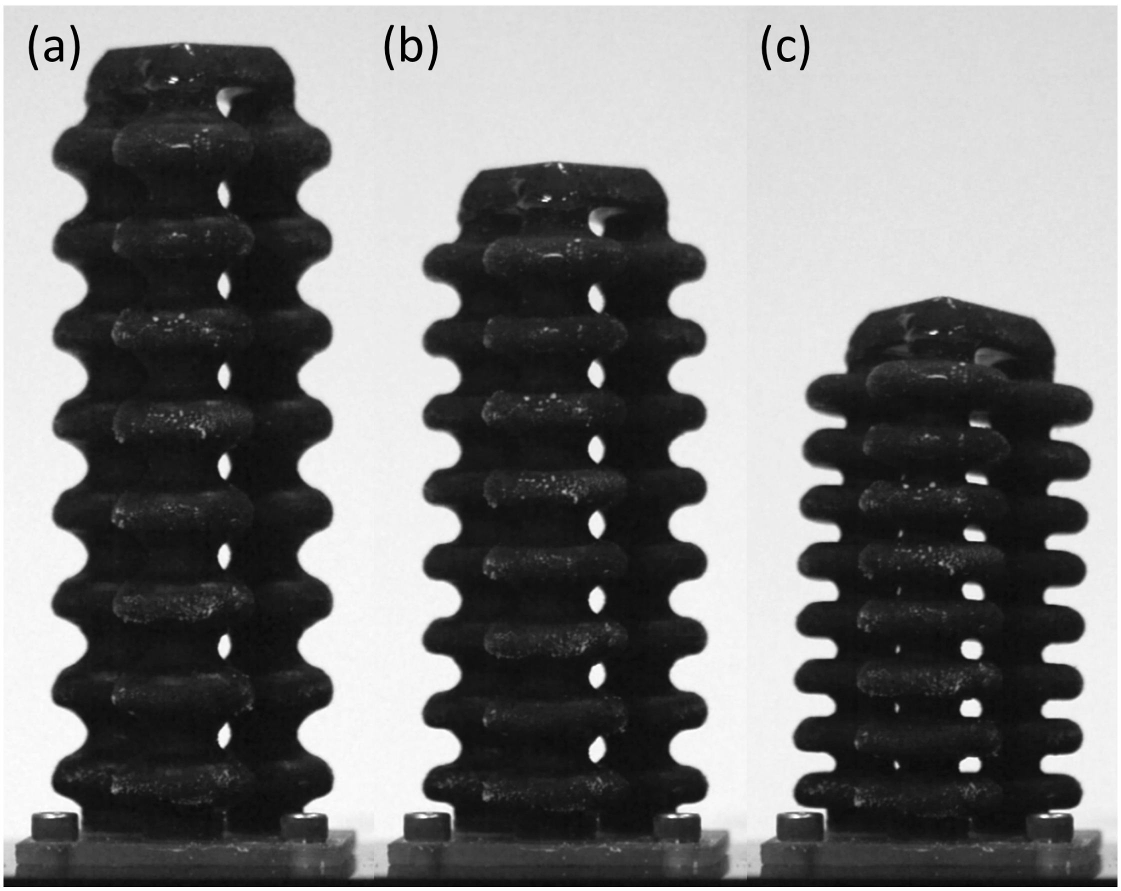

Figure 2.6: Actuator linear displacement. a) Three chambers inflated to 69 kPa. b) Three chambers at 0 kPa. c) Three chambers at -60 kPa.

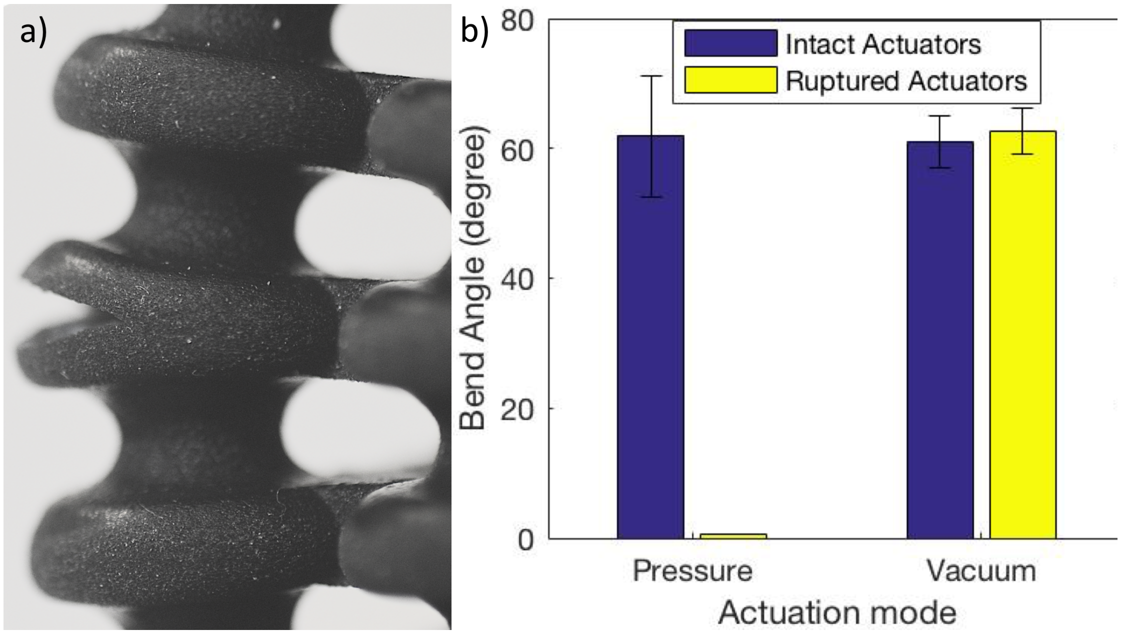

Figure 2.7: a) A rupture created on the actuator due to delamination of the 3D printed layers. b) Actuator's bend angle comparison for different actuation with ruptured and intact actuators (error bars represent standard deviation)

2.3.4 Operation of Ruptured Actuators with Negative Pressure Actuation

The most frequent failure mode for the 3D printed actuators is delamination of printed layers (Fig. 2.7a). Because 3D printing works by laying down successive layers of material, the strength of a part perpendicular to these layers is typically lower than the strength parallel to these layers. For this reason, I wanted to investigate an approach to recovering operation of ruptured actuators. For this experiment, I repeated the output force test and the bend angle comparison experiments for operation using only vacuum at -69 kPa and operation using only positive pressure at 60 kPa.

The ruptured actuators which I tested with negative pressure did not show any sign of failure and their performance was at par with the undamaged actuators. On the other hand, the ruptured actuators I tested with positive pressure recorded 0 degrees bend angle and 0 N blocking force due to the air leakage through the rupture. (Fig. 2.7b) shows the actuators bend angle comparison for different actuation with ruptured and intact actuators.

2.3.5 Hand Writing Demonstration

To test the capabilities of the volumetric control system, I demonstrated the control of a soft actuator performing a continuous motion in the form of hand writing of text. I attached a laser pointer to the tip of the actuator in the axial direction to map the position of the tip to a planer sheet of paper (see Fig. 2.8 and supplementary video). A webcam was used to track the position of the laser pointer projected onto a sheet of paper. Closed loop control of the system relied on pressure feedback alone (i.e. without visual servoing).

To achieve an accurate continuous motion, I implemented a time delay between reference points along the actuator path to allow the actuator to complete its time dependent deformation caused by the viscoelastic 3D printed material used to print the actuators. Algorithm 1 summarizes the control algorithm used and the complete code is attached in [Appendix B].

Import set of reference pressures for each point in the trajectory of the actuator. ;

while *actuator's path is not complete* **do**

Calculate the error of the pressure;

if *not all three chambers are at their respective reference pressures.* **then**

Correct error of the pressures using PID controller ;

else

Wait ten seconds for the material to relax. ;

end

Move to next reference point.

end

Algorithm 1: Differential Pressure Actuation for Trajectory Control of Viscoelastic Actuator

The letters produced following the above algorithm were displayed on a monitor (Fig. 2.8). The letters are connected since I did not control the on/off state of the laser. The precision of the system was demonstrated by repeating the same writing multiple times; the second loop exhibited a maximum deviation of 1.8 degrees from the first loop, and subsequent loops were almost indistinguishable from the previous iterations.

2.3.6 Suction Cup Manipulation Demonstration

A primary advantage of differential pressure control is the ability to extend and retract the actuator as demonstrated in the workspace comparison experiment. I devised a demonstration to exemplify a potential usage for this axial extension in soft robotics and the advantages of a control system with negative and positive pressure capabilities through a demonstration of grasping and manipulation of a fragile object (light bulb). I designed an actuator with a suction cup end effector that we actuated using a fourth syringe pump unit to apply a vacuum to the suction cup. The objective of the demonstration was for

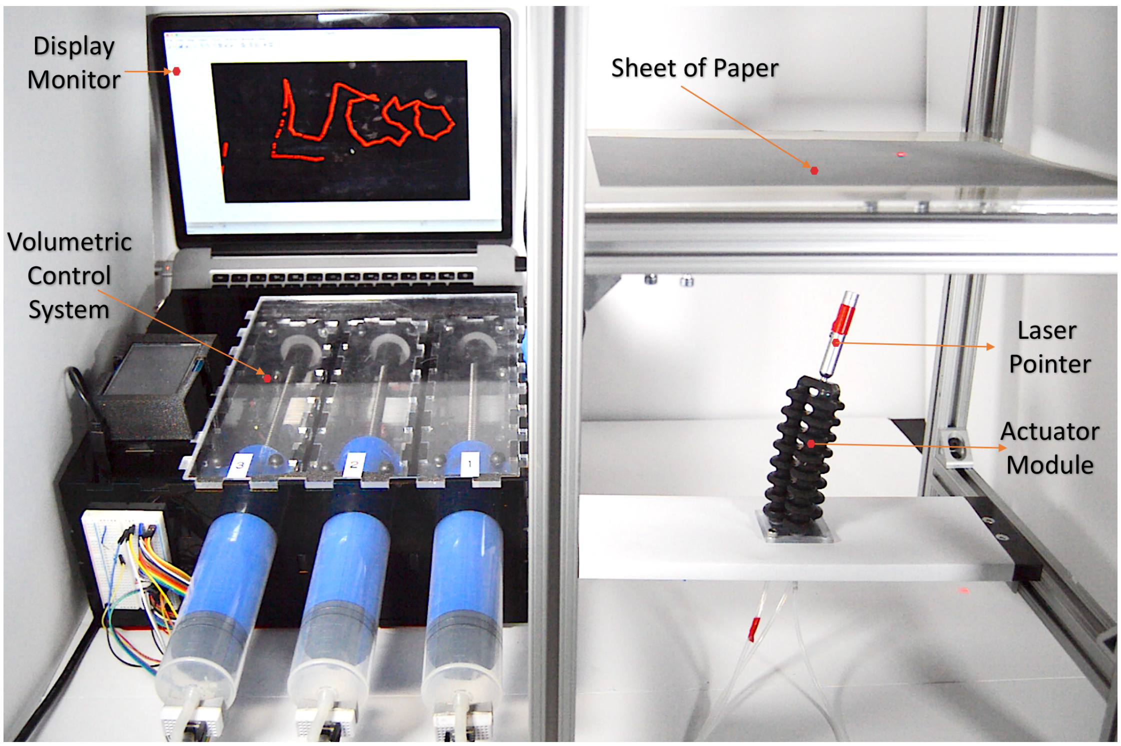

Figure 2.8: Hand Writing Demonstration Setup. I manipulated the actuator with a laser pointer at the tip of it in the axial direction and a web-cam (not displayed) was used to track the laser light

the actuator to approach the object, grasp it, complete a full rotation around the full workspace of the actuator and return the object to its initial position. The main challenge in the current demonstration were the carrying capacity and long-term manipulation caused by the limited sealing between the suction cup and the object (see Fig. 2.1a and supplementary video).

2.4 Finite Element Analysis of Differential Pressure Actuation

The bellowed actuator was simulated using the finite element method (FEM) software (ANSYS Inc. Mechanical) for actuation pressures up to 60 kPa (Fig. 2.9). The FEM model of the actuator is a surface model meshed with shell elements with the thickness of the actuator. The three actuation chambers are connected using beam elements. The experimental average bend angle was 79 degrees with a standard deviation of one degree. The FEM model simulation bending angle was much more conservative as it predicted a bending angle of 58 degrees.

The case with high vacuum pressure causes the bellows to collapse and come into contact with one another. As a consequence, the FEM analysis failed to converge for higher values of negative pressure due to the nonlinearities involved in the model. Alongside the material and structural non-linearities, the case with high vacuum pressure (i.e. less than -20KPa) also involves contact nonlinearities which inhibit convergence to a final solution using mixed (Normal Lagrange + Penalty) contact formulation. The FEM model uses beams to constrain the maximum diameter of the bellows together. In reality, the connecting members have some thickness which may affect the bending. Also, the material used for the bellow is viscoelastic. Due to the materials unknown viscoelastic properties, for the FEM model, I approximated the material as a hyperelastic with the

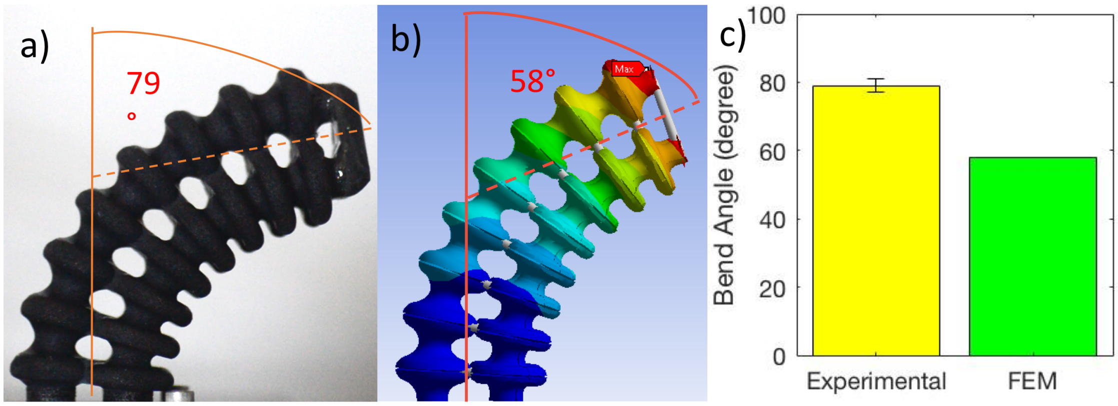

Figure 2.9: Bending angle comparison for experimental and the finite element model with 60 kPa in a single chamber and -30 kPa in the other two chambers. a) Experimental results bending angle of 79 degrees. b) Simulation results bending angle of 58 degrees. c) Comparison of bend angle results (error bars represent standard deviation)

Neo-Hookean material model. Hence, these two factors contribute to the discrepancies between the FEM model simulation and the experimental results. A further study of the FEM analysis of 3D printed bellowed actuators driven by negative pressure is left to future work.

2.5 CONCLUSIONS

In this chapter I demonstrated a volumetric control system for closed systems that utilizes differential pressure control for the actuation of soft modules. Our results show an increase of 54% and 43% in blocking force using differential pressure as compared to negative and positive pressure respectively. The results from our displacement test define the reachable workspace of the actuator bending angle and axial displacement. The improved three-dimensional workspace achieved by differential pressure control could enable a wide range of highly maneuverable soft robots capable of complex movements and precise trajectory tracking as demonstrated in our hand writing and manipulation experiments. I also demonstrated the self-healing characteristic of vacuum actuation of ruptured actuators which failed under positive pressure but regained normal operation under negative pressure. This feature could be used to improve the robustness and lifetime of 3D printed soft robots. Further work has yet to be done to improve of the positioning control of the actuators with a faster response time. Long term operation still represents a major challenge for 3D printed soft actuators due to material permeability and low durability. Experimental testing for lengthy continuous actuation is yet to be explored. Nonetheless, I believe that this work demonstrates the promise of using low-cost, modular, volume control systems to actuate 3D printed soft robots, and that this approach will lead to promising new applications of this emerging technology.

Chapter 2, in full, has been submitted for publication of the material as it may appear in (2017) ”Differential Pressure Control of 3D Printed Soft Fluidic Actuators”, Int. Conf. on Intelligent Robots and Systems (IROS), Vancouver, Sept. 2017. Kalisky T., Wang Y., Shih B., Drotman D., Jadhav S., Aronoff-Spencer E., and Tolley M T. The dissertation/thesis author was the primary investigator and author of this paper

Chapter 3

Human Centered Design for Biometric Identification of Infant for Vaccinations

Immunizations save millions of lives annually worldwide and are considered one of the most successful and cost-effective health interventions. Although the amount number of children who are vaccinated each year is continuously , many challenges remain in reaching all children: lacking or non-existing medical records, insufficient funding, and inefficient systems. One method to improve the vaccination process in vaccination clinics in low resources settings is a faster and more reliable system for keeping medical and vaccination records. In this work, I explore the development and use of a fingerprinting device for biometric identification of infants for tracking vaccination records. Prior attempts using adult biometric technologies for newborns and infants have met with limited success. The challenging iterative design process in this work was the limited access to infants for testing. We used a human-centered design approach and followed two parallel design iteration paths for contact and non-contact fingerprinting imaging techniques along with studying the many failure elements impeding high quality fingerprints. The non-contact device provided several advantages over the contact device in terms of overall consistency of print quality expressed in acceptance rate and in matching accuracy based on commercially available biometric software.

3.1 Introduction

As one of the most successful and cost-effective health intervention, immunizations are estimated to save over two million lives annually worldwide [38] and global coverage of immunization is at a record high with more than 100 million children vaccinated annually for diphtheria, tetanus, pertussis and measles among others [38]. Immunization programs around the world and particularly in developing countries, however, still face many challenges in reaching all children. A key factor in the current vaccination process is the time it takes to identify children and examine their medical records, especially in low resources areas where identification documents and medical records are not always available. There is a growing effort to build a viable biometric system and database that automatically identifies individuals and dynamically keeps track of their immunization record. Biometrics is the process of automatically recognizing a person using distinguishing traits [39].

In his work [40], Jain describes the fundamental biometrics characteristic requirements and main issues to be considered in biometrics system; These biometrics characteristics guided us in our design process for our system.

> What biological measurements qualify to be a biometric? Any human physiological and/or behavioral characteristic can be used as a biometric characteristic as long as it satisfies the following requirements:
>
> - Universality: each person should have the characteristic.
> - Distinctiveness: any two persons should be sufficiently different in terms of the characteristic.

- Permanence: the characteristic should be sufficiently invariant (with respect to the matching criterion) over a period of time.
- Collectability: the characteristic can be measured quantitatively.

However, in a practical biometric system (i.e., a system that employs biometrics for personal recognition), there are a number of other issues that should be considered, including:

- performance, which refers to the achievable recognition accuracy and speed, the resources required to achieve the desired recognition accuracy and speed, as well as the operational and environmental factors that affect the accuracy and speed;
- Acceptability, which indicates the extent to which people are willing to accept the use of a particular biometric identifier (characteristic) in their daily lives;
- Circumvention, which reflects how easily the system can be fooled using fraudulent methods.

There are a variety of off-the-shelf systems that qualify as effective biometric devices with varying degrees of success. The human eye (retina, and/or iris) is widely used by commercial systems [41]. Mostly implemented for security purposes, and considered highly accurate yet requires a high degree of cooperation and coordination e.g. keeping the eyes open for imaging. The iris and retina imaging is traditionally done through optical imaging sensors.

Still, perhaps the most common biometrics characteristic is the fingerprint; previous work has been done with a plethora of fingerprinting systems that uses CMOS capacitance [42, 43], optical imaging [44, 45], and ultrasound [46, 47]. Other characteristics that are currently being used are facial recognition [48], palm print [49, 50], vein imaging [51], and thermograms [52]. A full table of all biometrics characteristics and their quality metrics is attached at [Appendix C.2]. When it comes to biometrics identification of infants, no system is completely reliable. Current technologies fall short with the main properties of biometrics characteristics [See table 3.1]. Eye scanning for infants, although technologically feasible, presents a cooperation challenge as the infants eyes need to remain open for successful imaging. It also presents an accessibility challenge as it is often conceived to be invasive by caregivers.

Table 3.1: Biometrics Traits

Biometric Trait	Required Degree Of Subject Cooperation	Persistence	Parental Concerns	References for Attempt with Infants
Face	Moderate (Stare Towards Camera With Neutral Expression)	Low (Facial Aging)	Minor	[53]
Iris	High (Open eyes and stare towards camera)	Potentially high	Major (IR illumination, obtrusive capture process)	[54]
Palm-Print	Moderate (Open fist and allow operator to hold the palm	Potentially high	Moderate	[55]
Foot-Print	Low (removal of shoes and socks and allow operator to hold foot	Unknown	Minor (Used in U.S. hospitals)	[55]
Ear	Low	Potentially high	Minor	[56]
Palm-Vein Pattern	Moderate (Open fist and allow operator to hold the palm	Potentially high	Moderate	[57]
Fingerprint	High (Allow the operator to hold the childs finger	Potentially high	Moderate	[58]

Previous work has also been done to develop other infants biometrics systems. Fields et al. [56] presented a new approach for ear recognition for infant identification and Tiwari et al. [59] demonstrated an algorithm with matching accuracy of 83.67%. Although very promising, ear recognition has not been studied over a long period of time to give sufficient evidence for permanence and current algorithm are not accurate enough. In a more recent work, Tiwari et al. [53] presented a novel method for infants biometrics identification using facial recognition combined with soft biometrics (gender, blood group, height, and weight). The method showed promising results but the soft biometrics and facial recognition are not permanent enough to allow for a long term reliable identification for immunization tracking. Palm-print and foot-print based biometrics have been studied by Weingaertner et al [55] . with captured print resolution of 1200 points per inch (PPI) and 2400ppi, this approach yield over 63% and 83% matching accuracy for foot-print and palm-print respectively. In contrast with eye scanning, parental level of acceptance with fignerprinting is usually much higher as the process is completely non-invasive. The challenges with infants arise mostly in the context of current fingerprinting technology: not only are newborns fingers 2.6 times smaller than adults fingers [ref both hand studies] and the ridge distance in a newborns fingerprint is approximately 3-4 times smaller than adults [[60]] but their skin is much more elastic and more easily deformed or flattened in contact with a flat surface. Most adults fingerprint system capture prints at resolution of 500ppi whereas studies have shown that to achieve high quality infant fingerprint a much higher resolution is needed. Jain et al. [61] presented promising results for infants fingerprinting with a 1270ppi print resolution capture using CMOS sensor developed by NEC [62] exhibiting true accept rate (TAR) matching of 43.43% for infants younger than 4 weeks.

In this chapter, I present and test a new a finger/palm print biometric system to be implemented in vaccination clinics in developing countries. Our approach was to test existing technologies, and study their failure modes (wrinkles, deformation, flattening, rolled, fingers, low, resolution). our next step was to prototype possible solution for the critical failure modes using human centered design and run forward with lead devices that resolved failure elements and produced high quality prints. Our human centered design approach resulted in two leading to two parallel prototyping trajectories [Fig. 2.6]; the first was the more traditional fingerprinting technique where the fingerprint part of the finger comes in direct contact with the imaging device which leads to a levelled fingerprint imaging plane. The customary contact fingerprinting method causes fingerprint deformation in infants which inspired our second design trajectory, non-contact imaging. Non-contact fingerprint imaging, as its name suggests, means the fingerprint portion of the finger is not in contact with the device or any other surface during the imaging capture. This approach eliminates many of the fingerprint deformations caused by contact imaging but leads to other challenges such as curved fingerprint surface on the one hand, and a more difficult interaction with the finger which requires the motionless position of the finger without the help of a contact surface.

3.2 Methods / Approach

3.2.1 Testing of Existing Technology

The first step of the design process was benchmarking using off the shelf capture devices: I tested the Lumidigm V-Series V302 IP65 [ref data sheet] which utilizes Multispectral-Imaging (MSI) to achieve a very detailed and high resolution fingerprint and the Secugen Hamster IV (HSDU04P) which is FBI Certified PIV Single Finger Capture Device Compliant. Both devices were tested with infants between two to sixteen months old. I studied the ways in which both devices failed to produce high quality fingerprints and designed our prototypes to address these issues.

3.2.2 Design Evolution Approach Taxonomy

My approach followed two parallel design paths, contact and non-contact fingerprinting see [Fig. 3.1]. The advantages of contact fingerprint imaging are that the finger rests on a planer surface which provides support for the finger and helps restrain the finger in the correct imaging distance and position while also requiring a smaller depth of field (DOF) which makes the imaging system simpler. On the other hand, Infants fingerprints are so shallow and deformable that any contact with imaging surface create distortion in the print [63], especially with the excess movement of uncooperative infants. With non- contact imaging, the main advantage is with the unobstructed prints. However, this comes with the price of a curved print imaging surface, which requires a large DOF and a more complicated lighting configuration. Furthermore, non-contact fingerprinting of infants also pose a challenge in stabilizing the finger within the imaging region.

3.2.2.1 Contact

Contact fingerprinting can be done in several ways, we explored five different approaches as can be seen in [Fig. 3.1]. First off, Ultrasound: a very promising new technology that utilizes sound waves to map the fingerprint features and is been recently implemented in cellular devices. Although ultrasonic scanners produce high quality print in adults, we found that when it comes to newborns and young infants the systems resolution was insufficient. The second method which produces great results in adults uses total internal reflection (TIR). TIR is used to achieve optical transmission and reflection with a large dynamic range. [64]. Yet the elastic nature of the infants skin fails to produce satisfactory prints for identification. The third technique consisted of a hand-fitting spherical lens with a camera to image it from the opposite end. This would facilitate an ergonomic interface with the infants hand for an easy interaction with

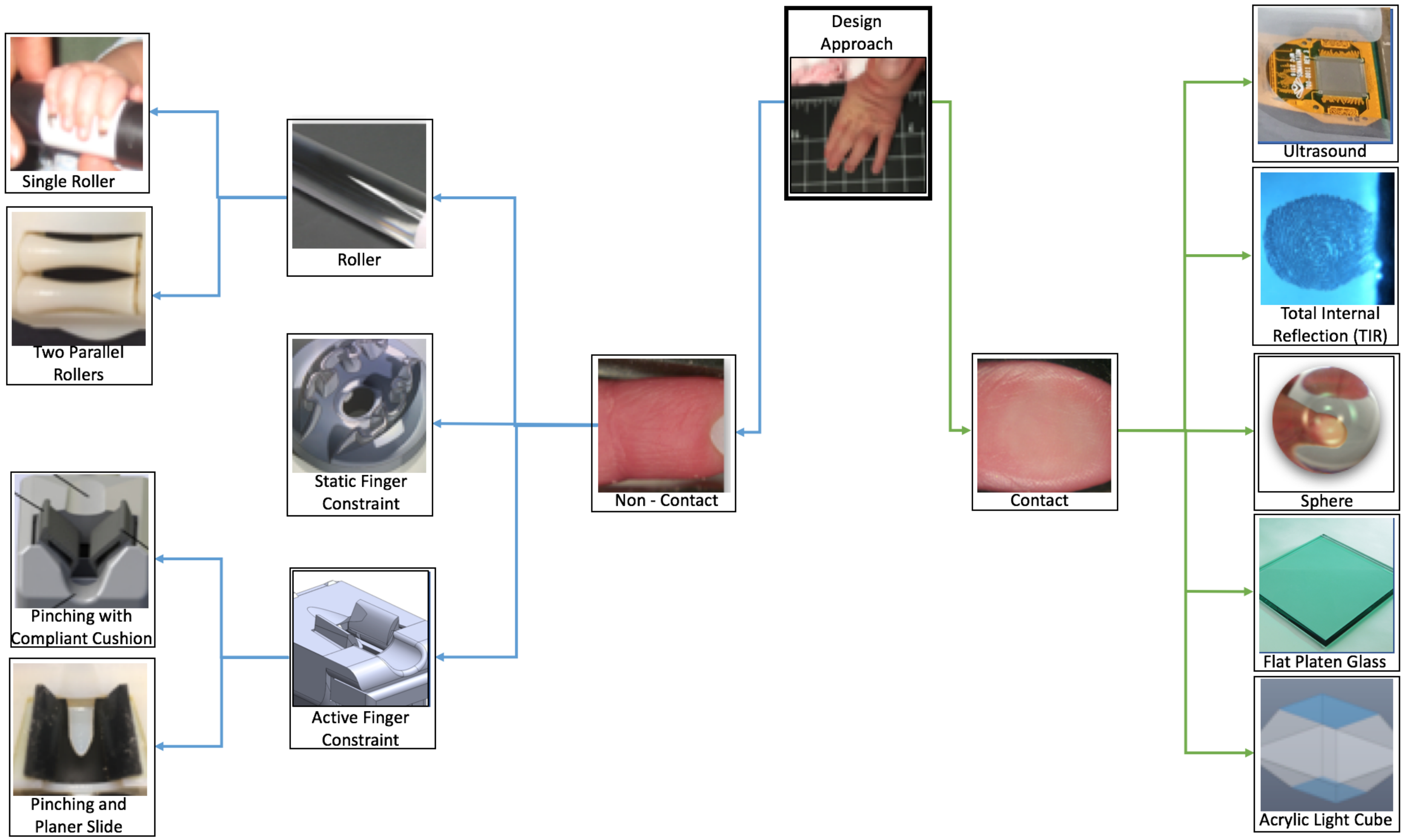

Figure 3.1: Design Evolution Approach Taxonomy; This figure illustrates the two approaches we took for fingerprint imaging. To the right is contact methods approaches. And to the left is the non-contact approaches.

the often uncooperative infant. Though the interaction was very promising, the image distortion through the spherical lens was too challenging to correct for a high-quality fingerprint. Next, we investigated a basic flat platen glass for a simple finger position and imaging. This approach resulted in a low-quality print due to the light refraction from the platen glass back into the imaging sensor. The last design approach was to convert the flat platen glass to the shape of a cube made of acrylic with angles just under the critical angle (with respect to the normal to the surface) of refraction of acrylic in order to prevent any unwanted light reflecting back into the imaging sensor. This method provided the highest quality prints of any of the contact methods and is the final contact approach used in this study.

3.2.2.2 Non-Contact

Non-contact fingerprinting for adult has been previously demonstrated in [65, 66]. There are two main advantages of non-contact fingerprinting over contact imaging. First is that there is no surface to obstruct the image or to refract undesired light between the finger and the imaging sensor which results in higher contrast between fingerprint ridges and valleys, and a higher quality print. Second is that the infant's skin is very elastic and the fingerprint are vary shallow so that the slightest pressure can deform the print. This method produces great results with adults as long as the hand is being held steadily in the air at the right position long enough for the fingerprint image to be taken. The main challenges with non-contact fingerprinting of infants is stabilizing the finger in the correct position for the duration of the image acquisition, and achieving a sufficient DOF to image the entire print on the curved surface of the finger. To overcome these challenges, we experimented with three configurations [Fig. 3.1]: The first was an oval shaped hole with static soft walls around it to guide to finger into the correct position. This method required a very simple design although due to variability in finger sizes, we manufactured several imaging holes in different sizes to adequately fit each finger. In addition, the positioning of the finger still proved to be challenging even with the guiding walls.

To achieve a more stable finger placement, and to accommodate a large variance of finger sizes, we designed an active constraint mechanism with a clamping device and soft grippers to hold the finger in the correct position without harming or hurting the infant. One experimental design was with a compliance cushion in each side of the gripper to harmfully constrain the finger. Another approach included a sliding slot that levels the finger in the focal distance of the camera and then slides out of the FOV when the grippers are clamping on the finger. The gripper design proved to be inhibiting light from reaching every part of the finger which results in uneven lighting. This approach helped resolve the issue of the variability of finger sizes because the mechanism compresses in on the finger and adopts to varying finger sizes.

The next configuration was an ergonomically shaped roller which enabled a rolling motion to lead the finger to the correct position. We tried two types of rollers: a single roller for the infants hand to grab, and two separate rollers with the finger positioned lengthwise between them and rolled into position. The single roller design proved too challenging because it required the entire imaging system to be completely encapsulated within the roller yet the roller needed to be small enough to fit in the hand of an infant. To improve on this method and still make use of the ergonomically shaped and functionally of the rollers, we transitioned to a two parallel rollers approach. In the two-rollers design, the finger could easily be rotated into the correct position when placed between the two rollers. The two-roller approach is the final non-contact design used in this study.

A matrix of the final hardware modules and nine of the selected interaction caps are shown in [Appendix D.1]..

3.2.3 Study Approach

In this study, we aimed to compare between our two-leading contact and non-contact imaging devices. All other features of the device were kept constant throughout the study. We had three participating infants where each infant partook in three fingerprinting sessions, with at least a week in between each session starting from as young as nine days for the first session and up to four months for the last session. Every subject was assigned an InfantIDNumber. The three subjects participating in this particular study are KP012, KP014, and KP015. For every finger, we captured three bursts of three images each resulting in nine fingerprint captures for each finger. The fingers are named in the with the following scheme LeftOrRight-FingerNumber, for example: left thumb is L0, where right middle finger is R2. The entire process was repeated twice with both contact and non-contact devices.

3.2.4 Image Processing Approach

Since there is no existing fingerprint matching software that is sophisticated enough to accept either color or monochrome images as input and successfully identify correct minutiae, it is crucial to develop an image pre-processing pipeline that can extract useful ridge information from finger images. In our project, we have different modules that take contact and non-contact finger images for research purposes. Although these two types of images are distinct from one another, their processing steps as shown in [Fig.3.2 a)] are similar.

3.2.4.1 Finger Image Extraction

The image first passes through finger extraction process that detect the Region of Interest (ROI) contains the finger. In our project, this process is done by using

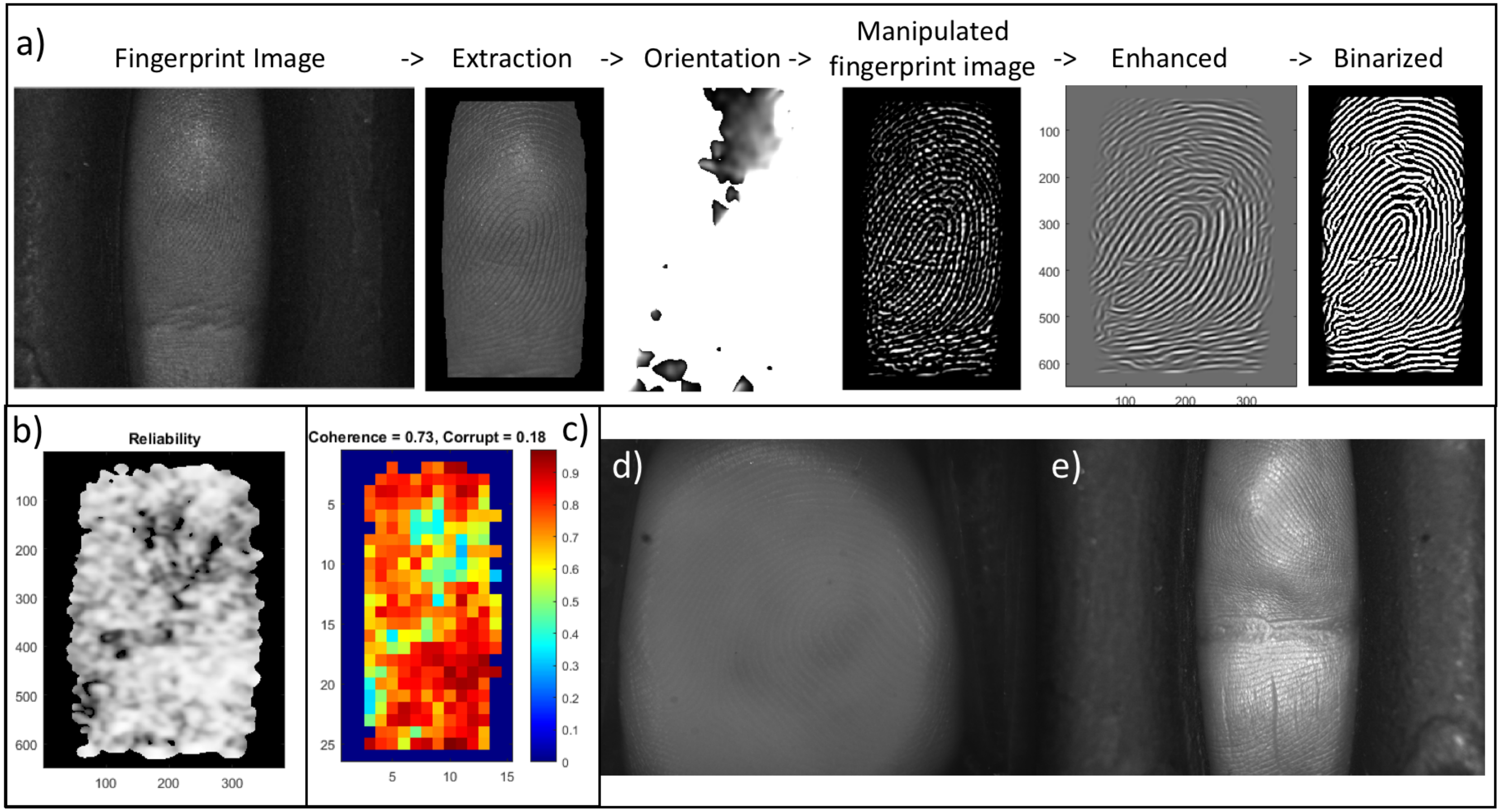

Figure 3.2: Fingerprint processing pipeline; a) Processing from raw image, to binarized image.b) Reliability Matrix. c) Coherence and corruption maps. d) Raw contact fingerprint. e) Raw non-contact fingerprint

the luminance channel from YUV color space under the assumption that all fingers have substantially higher luminance intensity than the background in both color and monochrome images. Once the finger image is extracted, it will be rotated such that the finger points upwards.

[Fig.3.2 d)] and [Fig.3.2 e)] are the example finger images from contact and non-contact devices respectively, and we can observe that contact finger ROI covers more area on the sides than the ones in the non-contact image. To normalize fingers captured from different devices, we crop the finger out with 1:1.3 width to height ratio for contact images and 1:1.5 width to height ratio for non-contact images, then resize the cropped finger into a suitable size with standard height of 500 pixels. This step is not only essential to reduce computational time in further process, but also ensure all fingers have similar ridge periods in all templates.

3.2.4.2 Fingerprint Orientation from Pixel to Orientation Map

To compute the fingerprint orientation, we must normalize the finger image to eliminate factors such as unbalanced lighting, shadow and uneven finger pressure. We first apply adaptive histogram equalization on the gray-scale image to eliminate lighting artifacts and improve the contrast between ridges and valleys. Then we use a median filter to reduce noise pixels and a 2D Gaussian kernel to smoothe ridges. After that, we perform morphological image reconstruction by connecting high intensity pixels in the image. The resulting fingerprint image is called the manipulated fingerprint, which aims to imitate latent fingerprints for commercial fingerprint matching software. A pixels orientation can be computed as the direction of the largest change in intensity in its neighborhood. Assuming a pixel lies either on a ridge or in a valley, the orientation of that ridge or valley is perpendicular to the orientation of the pixel. We partition the gray-scale image into 16 x 16 pixel blocks, and compute the orientations of all pixels in the block and compute the main overall direction for that block. All pixels in that block are then assigned that orientation. If the pixels in a block agree on the orientation, the block orientation is considered high quality. To quantify this, we calculate the area moment about the orientation axis found and compute the ratio r to the area moment around the perpendicular to this orientation. If this ratio is close to 1, the block pixels largely disagree and the block angle is not reliable. The block quality score is 1 - r. To best detect orientations, we manipulate the gray-scale image by contrast enhancement followed by noise removal and smoothing with median filter and a Gaussian filter, and finally subtracting the background. Since ridge orientations generally do not change abruptly, we correct spurious angle changes by applying a smoothing filter to the orientation map. In figure [Fig.3.2 a)] we can see the output of this stage, which is an orientation map (we compute a nice visualization for it), a reliability score for each block [3.2 b)], and the manipulated image which we computed the orientation map from. While it is possible to compute the orientation map directly from the gray-scale image, the map improves by the manipulation.

3.2.4.3 Ridge Enhancement

Here we apply oriented Gaussian filters to smooth out ridges in the manipulated image. The idea is that noise and pores in the ridges (and valleys) will be smoothed out by applying a filter in the direction of ridge. The kernel we use is a two dimensional elliptical Gaussian function with a small DC component subtracted. The DC subtraction aims at enhancing the contrast between valleys and ridges slightly. For speed, we convolute the entire image with the kernel oriented at a small number of orientations o evenly spaced between 0 and π. Then, for each o with corresponding convolution c we identify the blocks in the orientation map that are closest to this orientation and copy the corresponding blocks in c to the final output. In order to avoid abrupt changes in intensity across boundaries between blocks coming from different convolutions, we apply to each block copied a sinusoidal intensity adjustment where the offset is computed from the entire convolution.

3.2.4.4 Binarization and Skeletonization

The binarized image is obtained by thresholding the enhanced fingerprint, and it will be skeletonized by simply reducing the binarized ridge width to 1. As enhanced image is not perfectly smoothened, some small artifacts such as H-connected ridges, spikes and islands remain. These noise artifacts will be removed by specific kernels; otherwise, they will be captured by the minutiae detection algorithm, and result in many false endings and bifurcations.

3.2.5 Fingerprint Quality Evaluation

In this project, as we are frequently prototyping new modules to capture contact and non-contact infant finger images, it is therefore crucial to develop a fingerprint quality metrics to evaluate the performance of each module. In the industrial standard, NIST Fingerprint Image Quality (NFIQ) compliance from National Institute of Standards and Technology (NIST) is widely accepted as a reliable measurement of biometric quality [67]. NFIQ quantitatively rates fingerprint with quality score from 1 to 5, which in most cases can efficiently filter out poor quality fingerprints. However, for research purposes, NFIQ score does not provide much useful information to help us identify the problem that causes failures. As a result, we develop several other metrics such as coherence, corruption and contrast to discriminate poor quality fingerprint regions that caused by either camera DoF, illumination or finger distortion.

3.2.5.1 Coherence and Corruption

Despite of fingerprint abrasion and creases, fingerprint ridges are usually smooth and continuous; thus, sharp orientation changes within small fingerprint regions often denote unreliable ridges. Coherence is defined as the norm of the sum of orientation vectors d divided by the sum of their individual norms; his scalar always lies in [0,1]; its value is 1 when all the orientations are parallel to each other (maximum coherence) and 0 if they point in opposite directions (minimum coherence) [68] The gradient-based approach of the local coherence map can be expressed as:

$$coherence(\theta) = \frac{\lambda_{max} - \lambda_{min}}{\lambda_{max} + \lambda_{min}} = \frac{\sqrt{(G_{xx} - G_{yy})^2 + 4G_{xy}^2}}{G_{xx} + Gyy}$$

here λ_{max} and λ_{min} are the first and the second eigenvalues from the image gradient field, and G_{xx}, G_{yy} and G_{xy} are the covariance of the gradients. As coherence is approached based on image gradient field, it has high noise sensitivity around near-zero gradient regions such as ridge tops and valley bottoms. To dampen the noise influence, orientation vector field must be smoothened before computing the coherence. In our project, we use window size 25 to compute local coherence map [see Fig. 3.2(c)]. As each block will be assigned with a coherence score, we can compute the percentage of corrupted region in the fingerprint by counting the number of blocks that is lower than a certain coherence threshold (coherence $<$0.5). However, if the corruption percentage is over 40%, it will be very likely that there is not enough reliable minutiae in the fingerprint, even though it might have a relevantly high coherence.

3.2.5.2 Contrast

Since infant fingerprint ridges are much shallower than adults', it is difficult to extract reliable ridges from the captured image if the contrast is very low due to low signal to noise ratio. To compare the contrast performance from different modules, we developed a block-based image contrast assessment. First, we divide the captured image by the Gaussian blurred image to obtain the flatten image without luminance variation. Then, we perform line scan normal to the local orientation field based on 100x100 window. If the contrast is high, we can observe a clear sinusoidal signal in the spatial domain. In our case, each line scan is around 100 pixels, and infant ridge period is about 15 pixels. Due to the limited data length, we apply Welchs power spectral density (PSD) [69] estimate by truncating the line scan data into segments and using windowed periodogram to get the average. Finally, we extract the dominant period (1/frequency) and its corresponding PSD. To quantify the overall image contrast, we take the median from all dominant PSDs and periods. As we assume the dominant frequency in each window is from fingerprint ridges, the median period should lie around 15, and the larger the median PSD the higher the contrast. If not, the image will be determined as bad.

3.3 Results

3.3.1 Understating Failure Modes

A successful fingerprint capture requires a combination of many different conditions. A failed fingerprint in this context is a poor print capture that exhibits low contrast between ridges and valleys and/or low NFIQ score, which eventually results in low matching success rates. Throughout the design process we found a large variance in print quality with constant system setup and same fingerprinting subjects. For each print capture there are many unique features that affect the final print quality yet cannot be tested in isolation. I arranged all of the observed failure modes in in a fishbone diagram [Fig.3.3] which are organized into four main categories: finger/hand, interaction, imager, and illumination. Each represent a recognizable part of the fingerprinting process and can cause distinct failures. [Fig. 3.4] shows correlating examples of failed fingerprints and features. Each sub-figure correlates to the matching group letter from Fig.3.3.

Group (a) in [Fig.3.3], finger/palm, refers to any condition and characteristics of the infants hands and fingers. Small hands and fingers, as well as shallow and deformable prints laid out on a curved finger surface are all characteristics that will lead to poor quality print if the imaging system has insufficient resolution or too low depth of field (DOF). Other causes of poor quality prints related to finger and the palm are those that result in low number of minutiae or false minutiae finger and hand: wrinkles, peeling skin, injury to the print portion of the skin, wet or dry hands. The corresponding sub-figure [Fig. 3.4 (a)] provides two example of failures in print capture due to finger characteristics: [Fig. 3.4 (a1)] demonstrates a wrinkled finger and [Fig. 3.4 (a2)] shows dried, peeling skin which can register false minutiae.

The next group of failure modes, (group (b)) incorporate anything that happens during the interaction between the infant, the caregiver and the device. Infants do not willfully cooperate with the process, they tend to pull away from the device, close their fists hard on purpose or due to grasp reflex, or simply cry which leads to increased stress levels in the parent and the caregiver. Even when the infant is not actively resisting the process, it is challenging to align the finger in the right positing and orientation, due to the small scale of the infants hand and finger compared with the size of the fingerprinting device, and the cables that are attached to it. [Fig. 3.4 (b)] provides examples for interaction failures: [Fig. 3.4 (b1)] shows a failed fingerprint attempt with a curled finger and [Fig. 3.4 (b2)] shows the interaction of a curled finger and the device.

Group (c) [Fig. 3.3 (c)] lists the imager system failures. The imager system consists of a Complementary metal oxide semiconductor (CMOS) imager sensor and an optical lens. The configuration and quality of the two elements are crucial to achieve a high-quality print. A high-resolution imaging sensor placed near the finger is required to achieve an image with sufficient pixels per inch (PPI). To match the number of pixels per fingerprint ridge of an adult fingerprint scanned with a 500 PPI sensor, a minimum of 2000 PPI is required. Although we found that this requirement is not enough for a good quality print. Due the the deformable nature of the infant's skin a much higher resolution is needed based on our results, we set the resolution we set the resolution requirements to 3500 PPI. A large enough DOF is required to capture a high-quality fingerprint, especially with the non-contact technique. A low DOF can be caused by insufficient distance to the imaging sensor or by a small f number lens. Lastly it is important that the finger is inside the image field of View (FOV) which can be affected by the focal length of the lens and the size of the CMOS. [Fig. 3.4 (c)] illustrates failures in the imaging system. [Fig. 3.4 (c1)] shows a failed attempt at capturing a fingerprint of a 2-month-old using Lumidigm v302 [45], a commercially available system due to low resolution. [Fig. 3.4 (c2)] Is another example for insufficient resolution. [Fig. 3.4 (c3)] shows a failure due to shallow depth of field (DOF) and large field of view (FOV).

The last piece in the print failure sources puzzle is the illumination (group (d)) in [Fig. 3.3], which is directly linked to the imaging unit. The polarization of the light (cross or parallel) affects the contrast between the ridges and valleys of the print. Illumination angle through un-defused light can also lead to failure in the form of light hot spots that wash out portions of the print. Finally, the wavelength of the light also plays a role in imaging failures. Light in the red region of the color spectrum penetrates deeper into the skin compared with blue light. The light that penetrates the skin reflects with many polarizations and reduces the contrast between ridges and valleys. Illumination failure modes are shown in [Fig. 3.4 (d)]. Arrows 1 to 2 represents the path light will go from the light source to the imaging sensor with parallel polarization which eliminate any light which penetrate the skin from reaching the sensor. Arrows 1 to 3 represents cross-polarized imaging scheme which only partially eliminate light that penetrate the skin from reaching the sensor. Unpolorzied light reduced the contrast of the print. Light with wavelengths in the red spectrum penetrate deeper into the skin and reflects with undesired polarizations that affect print quality.

Finally, two samples with high quality fingerprints are presented in [Fig. 3.4]. [Fig. 3.4 a)] and [Fig. 3.4 b)] respectively, show highly detailed contact and non-contact infant fingerprints.

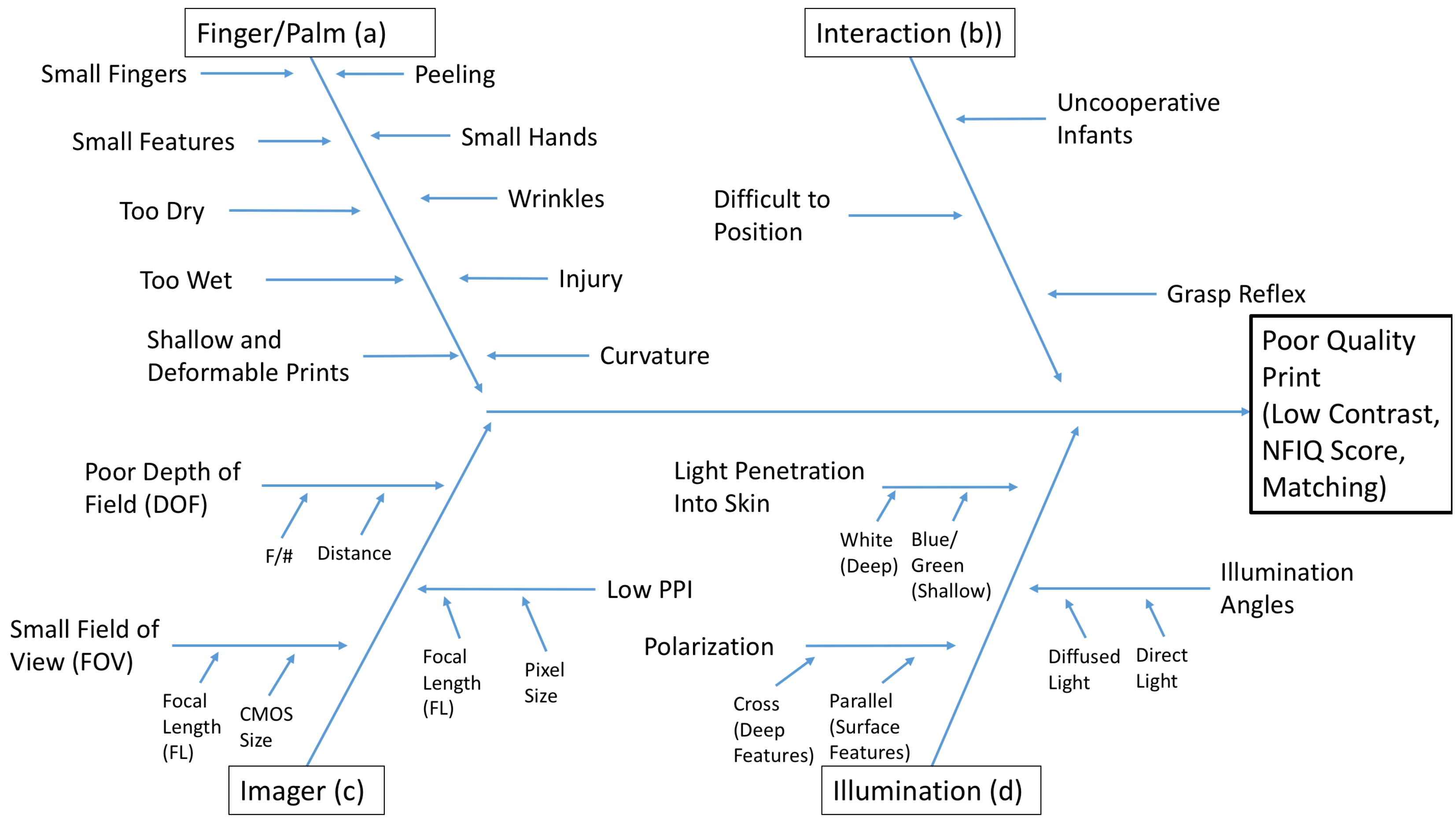

Figure 3.3: Fishbone diagram of causes to poor quality. Four main groups which incorporate features that lead to fingerprint failure. The four groups (a-d) correlate to the four sub-figures in [Fig. 3.4]

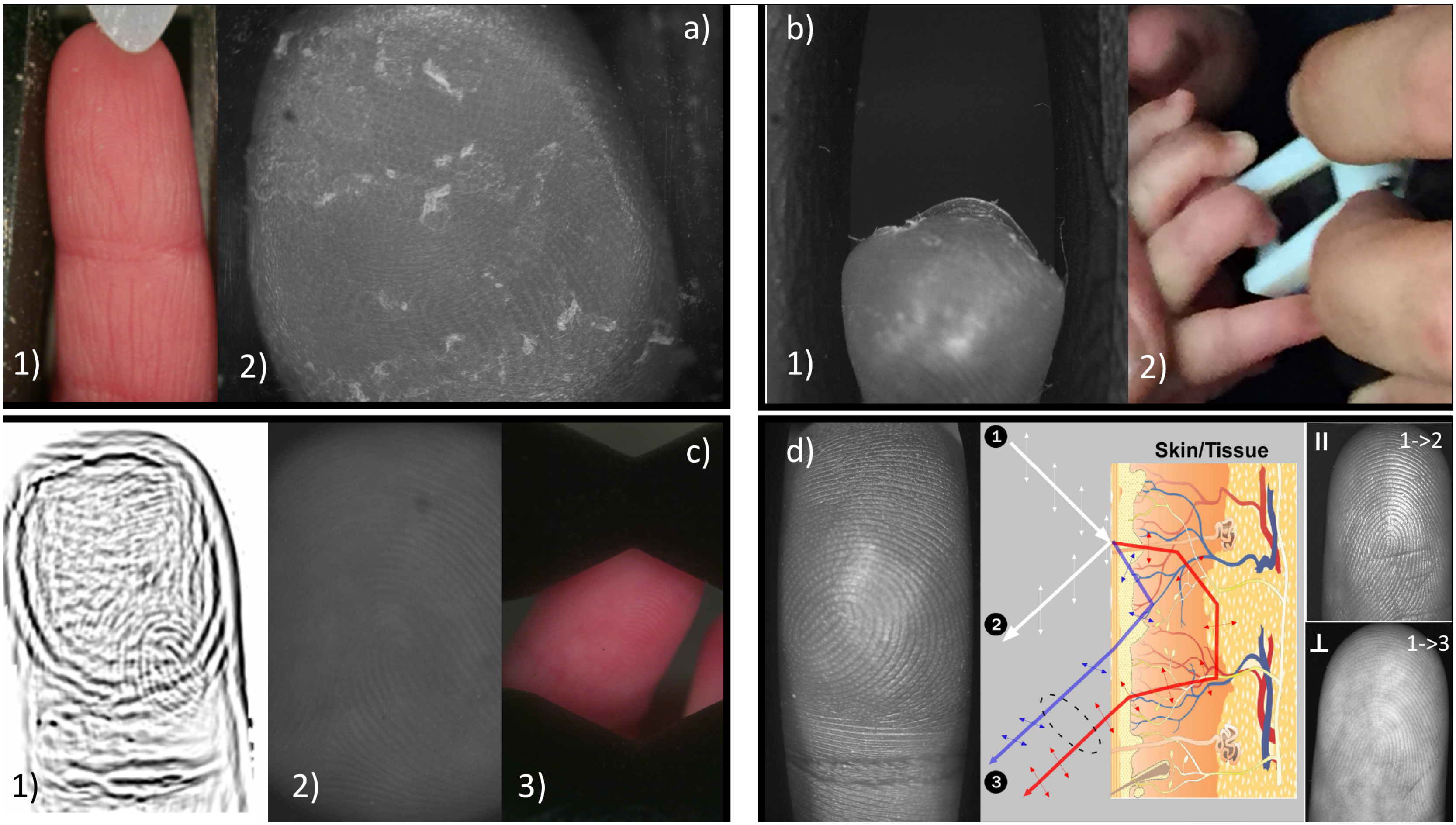

Figure 3.4: Example of failures in print capture; a) Examples of finger characterstics that cause poor printb)Interaction failures c) Imager system failures. d) Illumination failure modes

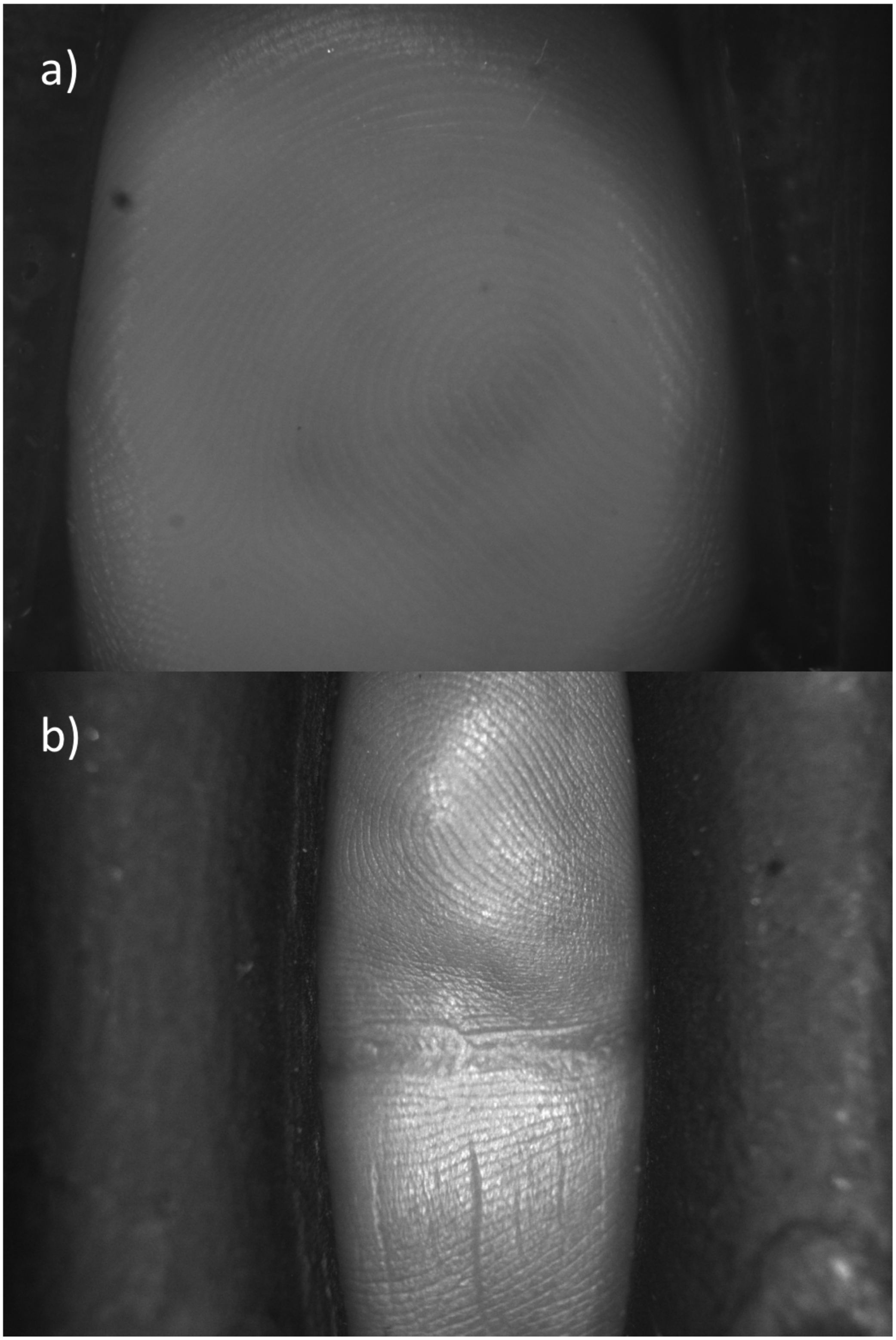

Figure 3.5: Two samples for high quality fingerprints: a) Contact fingerprint, b) Non-contact fingerprint

3.3.2 Data Analysis

In this project, we are using a commercial biometrics identification system Neurotechnology MegaMatcher SDK for our infant verification experiments. As MegaMatcher (MM)is specifically developed for adult fingerprint captured by optical and capacitive scanners, we have to preprocess our infant's finger images to make them similar to adult fingerprints that MM requires. The main difference between infant's and adult's fingerprints is finger size, but infants have higher ridge frequencies and shallower ridges. As MM also has its own image filtration algorithm to eliminate noises and corrupted ridges, we only use part of our fingerprint processing pipeline to obtain manipulated fingerprints. These fingerprints will be further downscaled to 500 PPI as pseudo fingerprint templates and then imported into MM. Besides our own quality metrics such as coherence and contrast, MM uses NFIQ and minutiae count as their image quality determination. If NFIQ score is Poor or number of reliable minutiae in the fingerprint is lower than certain threshold, that template will be rejected by MM. For each fingerprint matching experiment, we enroll multiple kids fingerprints from three longitudinal visits with up to nine templates per finger per visit.

First, we imported all the print captures from both contact and non-contact devices to MM and plotted in a bar graph the rejected and accepted images for each finger. The results are presented in [Fig. 3.6] and [Fig. 3.7] for contact and non-contact respectively. Each bar represents a single finger where the blue portion of the bars represents the accepted images and yellow the rejected images.

Once we have the accepted images in MM, we match images from each finger with multiple templates against all enrolled fingers, and a finger is correctly identified if any of its templates matches another template from a different visit. We then expand the total individuals, and repeat the matching process. The results are presented in [Fig. 3.8]

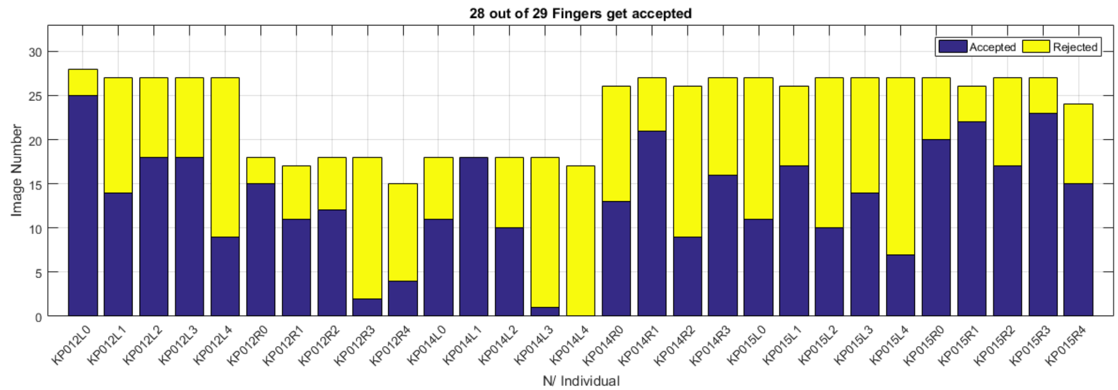

Figure 3.6: A bar graph of the accepted contact prints (blue) vs. the rejected prints (yellow)

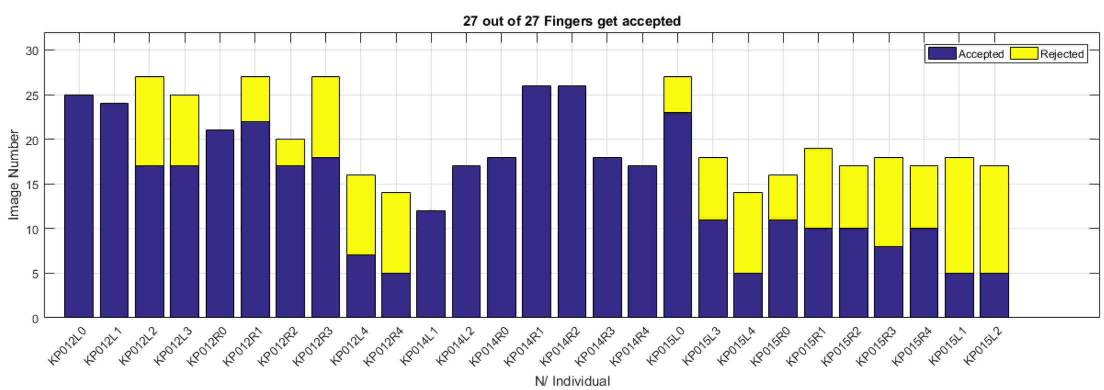

Figure 3.7: A bar graph of the accepted non-contact prints (blue) vs. the rejected prints (yellow)

and [Fig. 3.9] for contact and non-contact respectively.

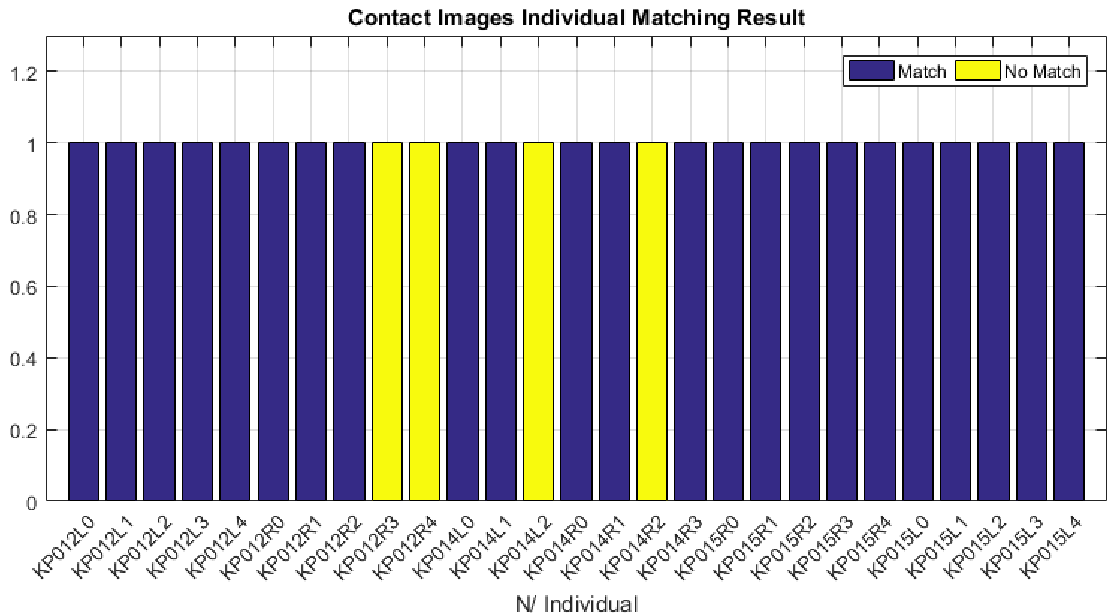

Figure 3.8: A bar graph of the matched contact prints (blue) vs. the rejected prints (yellow)

Next, we plotted the contact and non-contact fingerprint matching accuracy vs 1:N matching result from the three infants [Fig. 3.10]. In this case we treat each finger as an individual since every finger's fingerprint is unique; thus, three infants can have up to 30 valid identities.

Finally we plotted the same data set with matching accuracy vs. subject's age where the blue plot is for contact imaging and red is for non-contact [Fig. 3.11]. As the data is collected from three infants with three longitudinal visits, each dot in the figure indicates the mean matching accuracy from multiple fingers and plotted against the age of the infant at the time the image was captured.

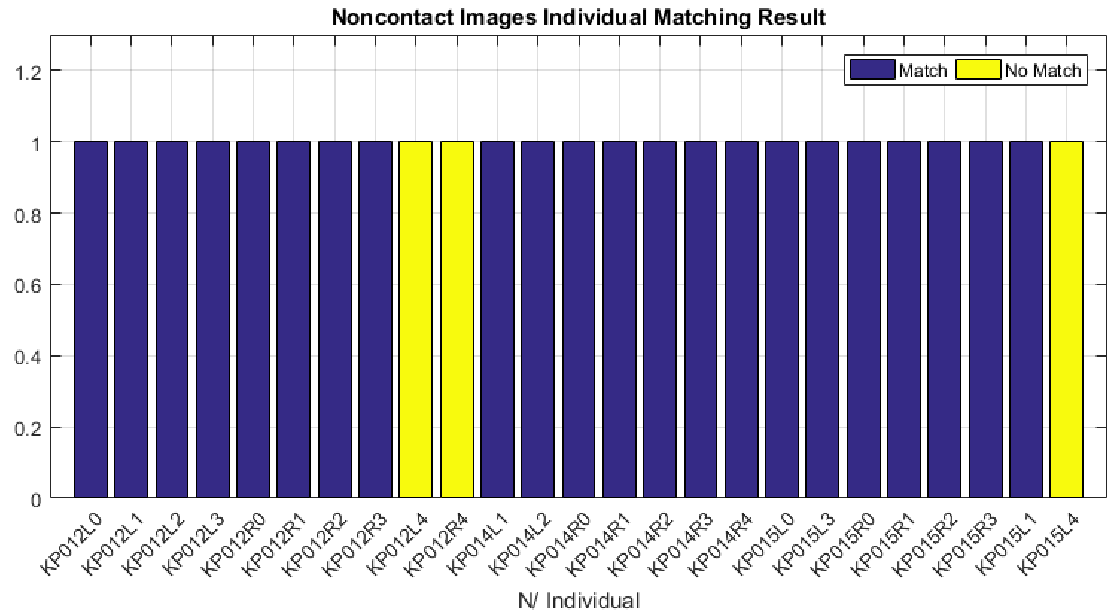

Figure 3.9: A bar graph of the matched non-contact prints (blue) vs. the rejected prints (yellow)

3.4 Discussion

From these results, we can first see that non-contact print captures were accepted at a higher ratio 2.99 accepted images for every rejection [Fig. 3.7], compare to only 1.27 accepted images for every rejected one with contact [Fig. 3.6]. This can be seen by the higher concentration of blue in the non-contact plot as compare with the content one. Notable information from the two plots [Fig. 3.6] and [Fig. 3.7] is that for contact there was one finger without accepted image where for contact all fingers had at least one accepted image. For the matching, the non-contact matched with a slightly higher matching accuracy with 22 out of 25 (88%) fingers matching as compared with contact where 23 out of 27 (85%) fingers matched. [Fig. 3.10] shows a better comparison of the accuracy vs the number of individuals for contact and non-contact. Although, the order of the individuals (fingers) was randomly selected and the trend is not as significant as the final data point. Ultimately, the plot for accuracy vs. the age of the subject [Fig. 3.11]

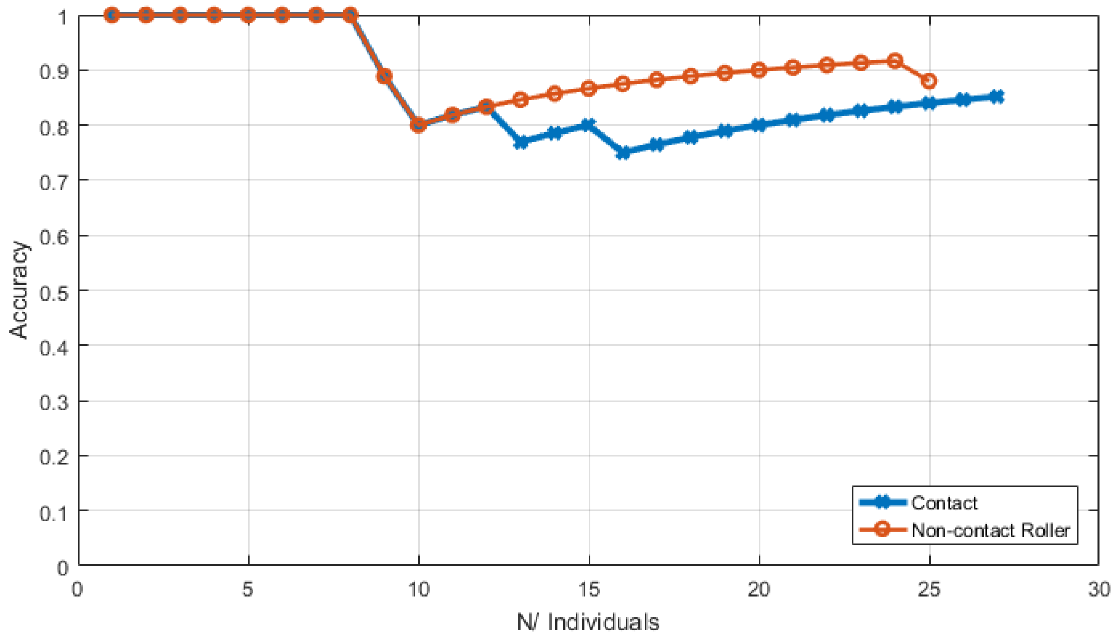

Figure 3.10: Contact (red) and non-contact (blue) fingerprint matching accuracy vs 1:N matching result from the three infants. Where is number of individual fingers.

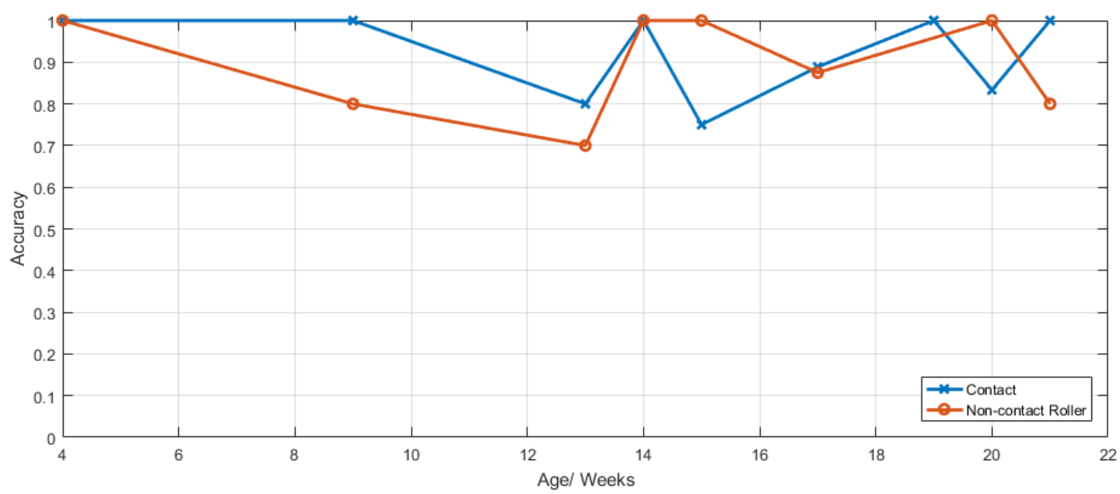

Figure 3.11: Matching accuracy vs. subject's age where the blue plot is for contact imaging and red is for non-contact.

shows that the contact device matches with higher accuracy in early age compared with the non-contact device. This trend becomes less significant over the age of 14 weeks.

3.5 Conclusion

From the results, we can conclude that the non-contact device produces more consistent high quality fingerprints which get accepted to MM much higher percentages, possibly due to favorable interaction of the device with the finger for a reduced contact induced print deformation. The data set used in this work is only a small snapshot of an ongoing longitudinal study and is insufficient to conclude which method is superior for matching in young age. Therefore, we yet abandon contact devices, and should continue testing with both for further in-depth analysis of the entire data base.

3.6 Future Work

Since we have very limited access to young infants for fingerprinting testing purposes which is a necessity progress evaluating and iterative design process, a scale replica of an infant finger be highly advantageous. I explored molding and casting technique to create a silicone replica of with highly detailed fingerprints. The challenge in making an infant size cast is that infants don't stay motionless long enough for the silicone to cure. I used a shrinking polymer, Hydrospan 400 [70] to cast a seven year olds hand which shrinks down to a newborn hand size, see [Fig. 3.12]. Yet even though the final cast is to scale, most of the fingerprint features did not transfer the repetitive process of molding and casting. Further work is yet to be done to optimize the process to produce an infants finger replica that will enable an accurate test-bed for fingerprinting lab testing.

Figure 3.12: Process of making a lifelike replica of an infant's hand with accurate fingerprint features. a) A silicone mold of a 7 year old. b) Same hand as in 'a' which was cast in Hydrospan and left to shrink. c) the shrunken hand model cast in silicone.

Chapter 3, in part is currently being prepared for submission for publication of the material. Kalisky; Tom; Forster, Deborah; Tolley, Michael T; Aronoff-Spencer Elaih. The dissertation/thesis author was the primary investigator and author of this material.

Appendix A

Starfish

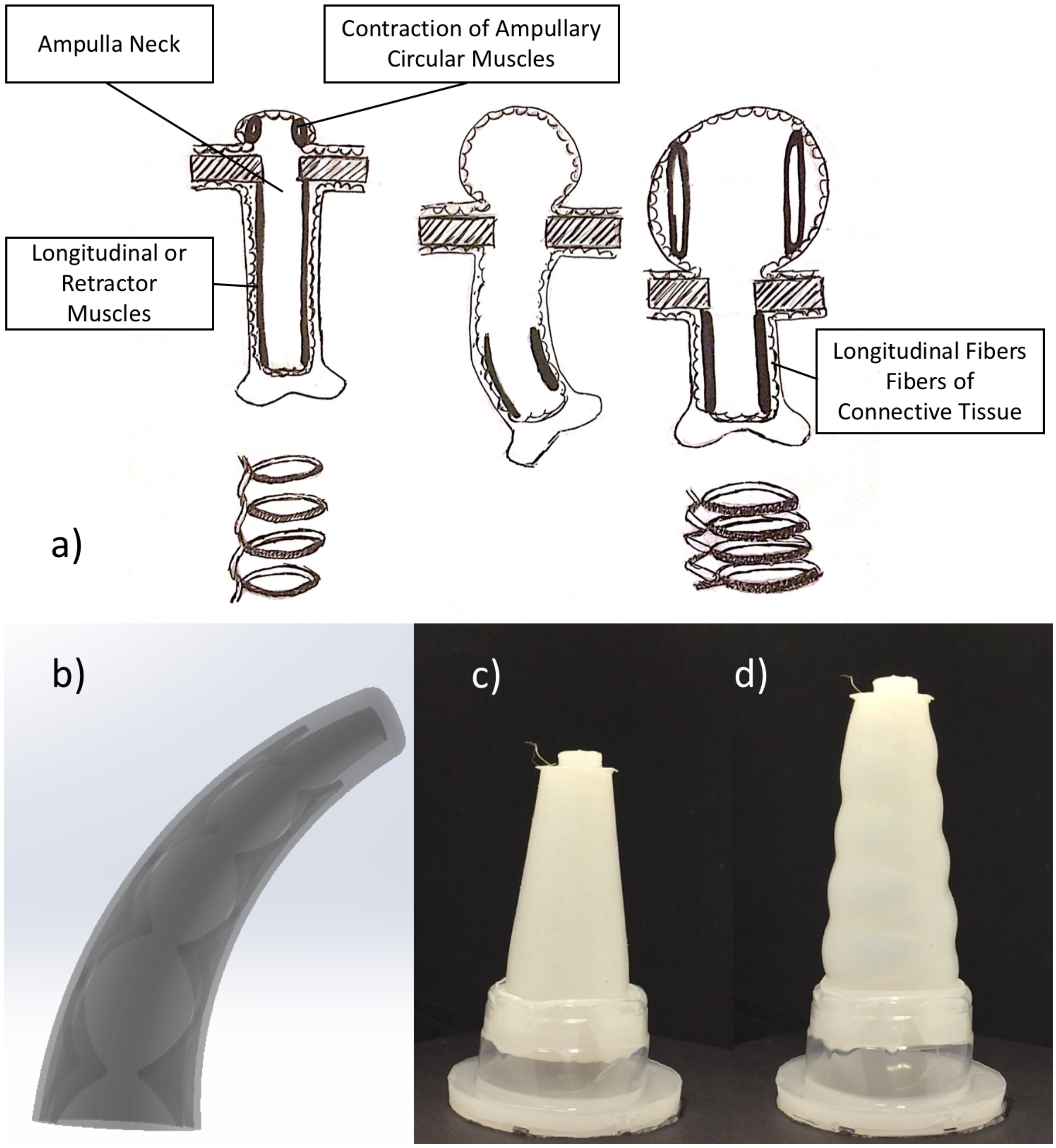

Figure A.1: a) A diagram showing a cut view of the locomotion of the starfish through contraction and relaxation of the muscle. b) A rendering of the proposed actuator with hydraulic chambers inside the outer walls which simulate the contracting muscles of the biological counter part to bend to actuator. c) Un-actuated silicone actuator designed. d) Elongation due to actuation of the central chamber. e) The volumetric control system for hydraulic actuation of soft robots.

Appendix B

Laser Drawing Code

```
//Pin intialization
// motor 1
  int  motor1_Enable_Pin = 43;
  int  motor1_Direction_Pin = 44;
  int  motor1_Clock_Pin = 45;
  int  motor1_Back_LS = 51;
  int  motor1_Forward_LS = 52;
  int  pressure_Sensor1_signal = A1;

//motor 2
  int  motor2_Enable_Pin = 46;
  int  motor2_Direction_Pin = 47;
  int  motor2_Clock_Pin = 12;
  int  motor2_Back_LS = 49;
  int  motor2_Forward_LS = 50;
  int  pressure_Sensor2_signal = A2;

//motor 3
  int  motor3_Enable_Pin = 13;
  int  motor3_Direction_Pin = 11;
  int  motor3_Clock_Pin = 10;
  int  motor3_Back_LS = 9;
  int  motor3_Forward_LS = 8;
  int  pressure_Sensor3_signal = A3;

void setup() {
  Serial.begin(250000);
```

```
  //Motor 1

  pinMode(motor1_Enable_Pin,OUTPUT);
  pinMode(motor1_Direction_Pin,OUTPUT);
  pinMode(motor1_Clock_Pin,OUTPUT);
  pinMode(motor1_Back_LS,INPUT);
  pinMode(motor1_Forward_LS,INPUT);

  digitalWrite(motor1_Enable_Pin,HIGH);

  //Motor 2

  pinMode(motor2_Enable_Pin,OUTPUT);
  pinMode(motor2_Direction_Pin,OUTPUT);
  pinMode(motor2_Clock_Pin,OUTPUT);
  pinMode(motor2_Back_LS,INPUT);
  pinMode(motor2_Forward_LS,INPUT);

  digitalWrite(motor2_Enable_Pin,HIGH);

  //Motor 3

  pinMode(motor3_Enable_Pin,OUTPUT);
  pinMode(motor3_Direction_Pin,OUTPUT);
  pinMode(motor3_Clock_Pin,OUTPUT);
  pinMode(motor3_Back_LS,INPUT);
  pinMode(motor3_Forward_LS,INPUT);

  digitalWrite(motor3_Enable_Pin,HIGH);

}

//inorout => 49 = pushing forwards
//inorout => 48 = pushing backwards
//inorout => 50 = stop
int inorout1=49;
int inorout2=49;
int inorout3=49;

//preallocation for deley value for varying motor speed with PID
float delay_val1 = 2000;
float delay_val2 = 2000;
```

```
float delay_val3 = 2000;

// PID Parameters
int Kp = 10;
int Ki = 0.05;
int Kd = 30;

//PID tolerance
int integralThresh = 1000;
float pressureThresh = 0.15;

//preallocation for integral values for PID
int integ1 = 0;
int integ2 = 0;
int integ3 = 0;

//set points for path following
const int numPoints = 48; // number of waypoints in the path.
float setpt1[numPoints] = {-1.75,-2,-1,
            1,.25,-.25,-.5,-1,-1,-.75,0,.5,.75,1,
            1.75,1.75,2,1.25,1,1.25,1.5,1.5,
            1.75,1.75,2,2.5,2.5,2.25,2.5,2.75,3.5,2.75,
            2.75,2.75,2.75,2.75,2.75,2.75,3.25,3.75,3.25,3.25,
            3.25,0,-0.75,-0.75,-1,-2};

float setpt2[numPoints] = {0,0,1.5,
            0.75,.75,.75,.75,.75,.75,.5,.25,.25,.25,.25,
            0.25,0.25,1.5,1.5,1.5,1.75,2,1.25,
            1.25,1.5,1.5,1.25,1.25,1.25,1.25,1.25,1.25,1.25,
            0.5,1,1.75,2,1.75,1,1,1,1,1,
            -2,-2,-2,-0.5,-0.5,-0.5};

float setpt3[numPoints] = {0,-1.75,-1.75,
            -2.75,-2.5,-2.25,-2.25,-2,-1.5,-.75,-1,-1,-1,-1,
            1.5,1,1,1,1.25,1.75,2.5,2.5,
            2.75,3.25,3.25,3.5,2.75,2.25,2,2.25,2.75,3,
            2.75,3.25,4,4.5,5,4.5,4.75,4,3.25,2.5,
            3.5,3.5,1.5,1,0,-1};

//preallocation for current pressure values
float curr1 = 0;
float curr2 = 0;
float curr3 = 0;
```

```
//preallocation for previous pressure values
float prev1 = 0;
float prev2 = 0;
float prev3 = 0;

//preallocation for error value between desired and current position
float err1 = 0;
float err2 = 0;
float err3 = 0;

//sum of all PID terms
float drive1 = 0;
float drive2 = 0;
float drive3 = 0;

//absolute value of drive variable
float drive1abs = 0;
float drive2abs = 0;
float drive3abs = 0;

//time passed since last step to be used for PID speed control
float timer1 = 0;
float timer2 = 0;
float timer3 = 0;

//compare timer with time_passed to evaluate elapsed time.
float time_passed1 = 0;
float time_passed2 = 0;
float time_passed3 = 0;

//flag for reseting motor stage
int reset_motors = 0;

//preallocation for input value - when input is 1 from serial
    after reset motors, program will start.
int run_stop = 0;

//pressure sensors parameters
int Vsupply = 5;
int Pmax = 150; //psi
int Pmin = 0;
```

```
//preallocation for elapsed time since all 3 units
    are at desired. pressures.
float SetPointTimer1 = 0;
float SetPointTimer2 = 0;
float SetPointTimer3 = 0;

//preallocation for is unit at desired pressure +- Threshhold.
int SetPointOn1 = 0;
int SetPointOn2 = 0;
int SetPointOn3 = 0;

//count for current set point number.
int count1 = 0;
int count2 = 0;
int count3 = 0;

// counter for moving initial starting point to middle of syringe
    for enabling vacuum use.
int stepCount = 0;


void loop() {

//Reset motors
//reset motor 1
if (reset_motors == 0){
while (digitalRead(motor1_Back_LS)==LOW ||
        digitalRead(motor2_Back_LS)==LOW ||
        digitalRead(motor3_Back_LS)==LOW){

        if (digitalRead(motor1_Back_LS)==LOW){
            digitalWrite(motor1_Enable_Pin,LOW);
            digitalWrite(motor1_Direction_Pin,HIGH);

            digitalWrite(motor1_Clock_Pin, HIGH);
            digitalWrite(motor1_Clock_Pin, LOW);
            delayMicroseconds(300);
        }

//reset motor 2
if (digitalRead(motor2_Back_LS)==LOW){
           digitalWrite(motor2_Enable_Pin,LOW);
           digitalWrite(motor2_Direction_Pin,HIGH);
```

```
            digitalWrite(motor2_Clock_Pin, HIGH);
            digitalWrite(motor2_Clock_Pin, LOW);
            delayMicroseconds(300);
        }

//reset motor 3
if (digitalRead(motor3_Back_LS)==LOW){

           digitalWrite(motor3_Enable_Pin,LOW);
           digitalWrite(motor3_Direction_Pin,HIGH);

            digitalWrite(motor3_Clock_Pin, HIGH);
            digitalWrite(motor3_Clock_Pin, LOW);
            delayMicroseconds(300);
        }
}

// Run the motors forward each by 400 microsteps.
    while (stepCount < 6000) {
      Serial.println(stepCount);
      // Move motor 1 forward by 1 microstep.
      digitalWrite(motor1_Enable_Pin, LOW);
      digitalWrite(motor1_Direction_Pin, LOW);

      digitalWrite(motor1_Clock_Pin, HIGH);
      delayMicroseconds(1);
      digitalWrite(motor1_Clock_Pin, LOW);
      delayMicroseconds(300);

      // Move motor 2 forward by 1 microstep.
      digitalWrite(motor2_Enable_Pin, LOW);
      digitalWrite(motor2_Direction_Pin, LOW);

      digitalWrite(motor2_Clock_Pin, HIGH);
      delayMicroseconds(1);
      digitalWrite(motor2_Clock_Pin, LOW);
      delayMicroseconds(300);

      // Move motor 3 forward by 1 microstep.
      digitalWrite(motor3_Enable_Pin, LOW);
      digitalWrite(motor3_Direction_Pin, LOW);
```

```
      digitalWrite(motor3_Clock_Pin, HIGH);
      delayMicroseconds(1);
      digitalWrite(motor3_Clock_Pin, LOW);
      delayMicroseconds(300);

      reset_motors = 1;
      stepCount++;
    }


if (Serial.available() > 0) {  // read the incoming byte:
                run_stop = Serial.read();
}
while (run_stop == 49){


  float pressure1 =
    (analogRead(pressure_Sensor1_signal)/1024.0*5.0 - 0.10*Vsupply)
    * (Pmax - Pmin) / 0.8 / Vsupply + Pmin;

  float pressure2 =
    (analogRead(pressure_Sensor2_signal)/1024.0*5.0 - 0.10*Vsupply)
    * (Pmax - Pmin) / 0.8 / Vsupply + Pmin;

  float pressure3 =
    (analogRead(pressure_Sensor3_signal)/1024.0*5.0 - 0.10*Vsupply)
    * (Pmax - Pmin) / 0.8 / Vsupply + Pmin;

  // motor 1 PID
        curr1 = pressure1;
        err1 = setpt1[count1] - curr1;

        if (abs(err1) < integralThresh){//prevent integral 'windup'.
            integ1 = integ1 + err1;//accumulate the error integral.
        }
        else {
            integ1 = 0; // zero if it's out of bounds.
        }

    float   P1 = err1 * Kp;
    float   I1 = integ1 * Ki;
    float   D1 = (prev1 - curr1) * Kd;
```

```
      drive1 = P1 + I1 + D1;

      if (0 < drive1){
          inorout1 = 49;
      }
      else if(0 > drive1){
          inorout1 = 48;
      }

      drive1abs = abs(drive1);
      prev1 = curr1;


// motor 2 PID
      curr2 = pressure2;
      err2 = setpt2[count1] - curr2;

      if (abs(err2) < integralThresh){//prevent integral 'windup'.
          integ2 = integ2 + err2;//accumulate the error integral.
      }
      else {
          integ2 = 0; // zero if it's out of bounds.
      }

  float   P2 = err2 * Kp;
  float   I2 = integ2 * Ki;
  float   D2 = (prev2 - curr2) * Kd;

      drive2 = P2 + I2 + D2;

      if (0 < drive2){
          inorout2 = 49;
      }
      else if(0 > drive2){
          inorout2 = 48;
      }

      drive2abs = abs(drive2);
      prev2 = curr2;


// motor 3 PID
      curr3 = pressure3;
```

```
    err3 = setpt3[count1] - curr3;

    if (abs(err3) < integralThresh){//prevent integral 'windup'.
        integ3 = integ3 + err3;//accumulate the error integral.
    }
    else {
        integ3 = 0; // zero if it's out of bounds.
    }

float   P3 = err3 * Kp;
float   I3 = integ3 * Ki;
float   D3 = (prev3 - curr3) * Kd;

    drive3 = P3 + I3 + D3;

    if (0 < drive3){
        inorout3 = 49;
    }
    else if(0 > drive3){
        inorout3 = 48;
    }

    drive3abs = abs(drive3);
    prev3 = curr3;


//Motor 1

if (inorout1 == 48){
    if (digitalRead(motor1_Back_LS)==HIGH){
      inorout1=50;
        //Serial.print("Y");
    }
    else {
       digitalWrite(43,LOW);
       digitalWrite(44,HIGH);
    }
}

if (inorout1 == 49) {
  if (digitalRead(motor1_Forward_LS)==HIGH){
    inorout1=50;
  }
```

```
  else {
    digitalWrite(motor1_Enable_Pin,LOW);
    digitalWrite(motor1_Direction_Pin,LOW);
  }
}

if (inorout1 == 50){
  digitalWrite(motor1_Enable_Pin,HIGH);
}


//Motor 2

if (inorout2 == 48){
    if (digitalRead(motor2_Back_LS)==HIGH){
      inorout2=50;
        //Serial.print("Y");
    }
    else {
       digitalWrite(motor2_Enable_Pin,LOW);
       digitalWrite(motor2_Direction_Pin,HIGH);
    }
}

if (inorout2 == 49) {
  if (digitalRead(motor2_Forward_LS)==HIGH){
    inorout2=50;
  }
  else {
    digitalWrite(motor2_Enable_Pin,LOW);
    digitalWrite(motor2_Direction_Pin,LOW);
  }
}

if (inorout2 == 50){
  digitalWrite(motor2_Enable_Pin,HIGH);
}


//Motor 3

if (inorout3 == 48){
    if (digitalRead(motor3_Back_LS)==HIGH){
```

```
          inorout3=50;
            //Serial.print("Y");
        }
        else {
           digitalWrite(motor3_Enable_Pin,LOW);
           digitalWrite(motor3_Direction_Pin,HIGH);
        }
    }

    if (inorout3 == 49) {
      if (digitalRead(motor3_Forward_LS)==HIGH){
        inorout3=50;
      }
      else {
        digitalWrite(motor3_Enable_Pin,LOW);
        digitalWrite(motor3_Direction_Pin,LOW);
      }
    }

    if (inorout3 == 50){
      digitalWrite(motor3_Enable_Pin,HIGH);
    }


// Delay and Run

    delay_val1 = map(drive1abs,1,500,500,1)/500;
    delay_val2 = map(drive2abs,1,500,500,1)/500;
    delay_val3 = map(drive3abs,1,500,500,1)/500;


          //Motor 1
  if(setpt1[count1]+pressureThresh < pressure1 ||
    setpt1[count1]-pressureThresh > pressure1){
  time_passed1 = micros()-timer1;
  if (time_passed1 >delay_val1){
  digitalWrite(motor1_Clock_Pin, HIGH);
    digitalWrite(motor1_Clock_Pin, LOW);
  timer1 = micros();
  }
}
  if(setpt1[count1]+pressureThresh > pressure1 &&
    setpt1[count1]-pressureThresh < pressure1){
```

```
    SetPointOn1 = 1;
  }


  //Motor 2
  if(setpt2[count1]+pressureThresh < pressure2 ||
    setpt2[count1]-pressureThresh > pressure2){
  time_passed2 = micros()-timer2;
  if (time_passed2 >delay_val2){
  digitalWrite(motor2_Clock_Pin, HIGH);
    digitalWrite(motor2_Clock_Pin, LOW);
  timer2 = micros();
  }
}
  if(setpt2[count1]+pressureThresh > pressure2 &&
    setpt2[count1]-pressureThresh < pressure2){
    SetPointOn2 = 1;
  }


 //Motor 3
  if(setpt3[count1]+pressureThresh < pressure3 ||
    setpt3[count1]-pressureThresh > pressure3){
  time_passed3 = micros()-timer3;
  if (time_passed3 >delay_val3){
  digitalWrite(motor3_Clock_Pin, HIGH);
    digitalWrite(motor3_Clock_Pin, LOW);
  timer3 = micros();
  }
}
  if(setpt3[count1]+pressureThresh > pressure3 &&
    setpt3[count1]-pressureThresh < pressure3){
    SetPointOn3 = 1;
  }


//motor check

  if(SetPointOn1 == 0 || SetPointOn2 == 0 || SetPointOn3 == 0){
    SetPointTimer3 = millis();
  }

  if(millis()-SetPointTimer3 > 3000){
```

```
    SetPointOn1 = 0;
    SetPointOn2 = 0;
    SetPointOn3 = 0;
    count1++;
    if(count1==numPoints){
    count1=0;
  }
  }


 Serial.print(pressure1);
  Serial.print(" ");
  Serial.print(pressure2);
  Serial.print(" ");
  Serial.print(pressure3);

Serial.print('\n');
}
}
```

Appendix C

A Detailed Biometrics Table

Biometric Matrix		Fingerprint	Finger Geometry	Palm Veins	Palm Print	Hand Geometry
Uniqueness	How differently and uniquely the biometri system will be able to recognize each user among groups of users	Fingerprints are usually considered to be unique, with no two fingers having the exact same dermal ridge characteristics.	**N/A**	The pattern of blood veins is unique to every individual	High Uniqueness	Unlike fingerprints, the human hand isn't unique. Individual hand features are not descriptive enough for identification
Accuracy	Consistancy of results to positively Identify Subject	Medium	Moderate	Moderate	Medium	Moderate
Speed	Amount of time it takes for machine read Biometric versus stored Biometric	9 to 19 (s)	3-5 (s)	3-5 (s)	N/A	3-5 (s)
Enrollment Time	Time required to enter new Biometric data	About 3 minutes 30 Seconds	1 Minute	N/A	N/A	1 Minute
Non-Match Rate	Probability that individuals who should be matched but are not matched by system	.2% - 36%	N/A	N/A	N/A	0% - 5%
False Match Rate	Probability of an erroneous mat in a single template compariso	0% - 8% approximately 1 in 100,000.	N/A	N/A	N/A	0% - 2.1%
User Acceptance	Physical, Psychological, and Cultural	Hygiene, Interaction	Hygiene, Interaction	Usage Difficulty	Hygiene, Interaction	Hygiene, Interaction
Factors Affecting Performance	Human or Measurment condition could adversly affect accurac	Dirty, Dry, Worn Fingerprints, Scratched Reader	Varying levels of growth hand injuries, swelling, and dexterity	Still not determined as unique as a fingerprint	Dirty, Dry, Worn Palm, Scratched Reader	Varying levels of growth, hand injuries, swelling, and dexterity
Variability with Ages / Permanence	Effects of age, if any, on subjects biometric identifiers	Stable	Stable, Howver accurac can vary depending o time between use	Stable	Stable	Stable, Howver accuracy can vary depending on time between use
Age of Stabilization	At what age is the features stabilizes consistent biometrics recognitio	By the time a fetus is six months old and approximately 12 inches in siz his fingerprints are fully developed	puberty	Palm vein patterns are formed during the first eight weeks of gestation in c manner, influenced by environment in a mother's womb. This is why the vei unique to each individual, even to twins. Veins grow with a person's skeletor reach a stable, "adult" pattern until growth stops. Consequently, patients usi may have to periodically re-enroll over time.	By the time a fetus is s months old and approximately 1 inches in size	puberty
Measurement Methods	Various Methods of Data Collection Available	Optical Methods -CMOS Capitacitance -Thermal Sensing -Ultrasound	Optical Imaging	Infrared Optic	Optical Methods -CMOS Capitacitanc -Thermal Sensing -Ultrasound	Optical Imaging
Cost	Relative Cost of technology	Low	Moderate	Moderate	Low - Moderate	Moderate

Figure C.1: Part A of a detailed table comparing the different characteristics of biometrics identifiers to assist in selecting the most appropriate identifier for each identification requirement.

Facial Recognition	Retina	Iris Recognition	Thermograms	Gait	Ear Recognition	Skin Reflection	Lip Motion	Oder/Scent	Heartbeat recognitio
The dimensions, proportions and physical attributes of a person's face are unique.	Iris recognition can perform 1: all matches in a high speed environment		N/A	N/A	Studies show that all ears of the investigated databases possess individual characteristics, which can be used for distinguishing between them. But because of the lack of a sufficiently large ear database, these studies can only be seen as hints, not evidence, for the outer ear's uniqueness.	N/A	N/A	N/A	??
Moderate	High	Hight	Medium	Low	Moderate	Medium to High	Moderate	High	??
10 (s)	3-5 (s)	Less than 1 (s)	Less than 1 (s)	15 - 30 (s)	3-5 (s)	9 - 19 (s)	10 (s)	3-5 (s)	??
2 -3 Minutes	1 Minute	1 Minute	1 Minute	N/A	1 Minute	About 3 Minutes 30 Seconds	2 -3 Minutes	1 Minute	??
3.3% - 70%	Low	1.9% - 6%	N/A	N/A	N/A	N/A	3.3% - 70%	Low	??
.3% - 5%	Almost 0%	.3% - 5% Iris recognition false accept rate is 1 in 1.2 million statistically	N/A	N/A	N/A	N/A	.3% - 5%	Almost 0%	??
Privacy	Seen as Intrusive, Usage Difficulty	Privacy, Usage Difficulty	Usage Difficulty	Usage Dificulty	Hygiene, Interaction	Hygiene, Interaction	Privacy	Seen as Intrusive, Usage Difficulty	??
Lighting, Orientation of Face	Disease, Equipment must used in close proximity	Glare, Reflections	Glares, Reflections	Motor Funtion Development, Injuries	Varying levels of growth	Dirty, Dry, Worn Fingerprints, Scratche Reader	Lighting, Orientation of Face	Disease, Equipmen must be used in close proximity	??
Stable	Stable	Stable	Stable	Questionable	Stable, Howver accuracy can vary depending on time between use	Stable	Stable	Stable	??
puberty	N/A	Its morphogenesis begins in the 3rd month of gesta and is largely complete by the 8th, although changes in pigmentation can occur during the first ye	N/A	puberty	ear has a rich and stable feature that is preserved from birth to old age	N/A	N/A	N/A	??
Optical Imaging Thermal	Infrared Imaging	Optical Imaging	Thermal Imaging	Optical Imaging	Optical Imaging	LED to Spectrometer	Optical Imaging Thermal	Infrared Imaging	??
Moderate	High	High	High	Moderate	Moderate	Moderate	Moderate	High	??

Figure C.2: Part B of a detailed table comparing the different characteristics of biometrics identifiers to assist in selecting the most appropriate identifier for each identification requirement.

Appendix D

Hardware Modules and Caps

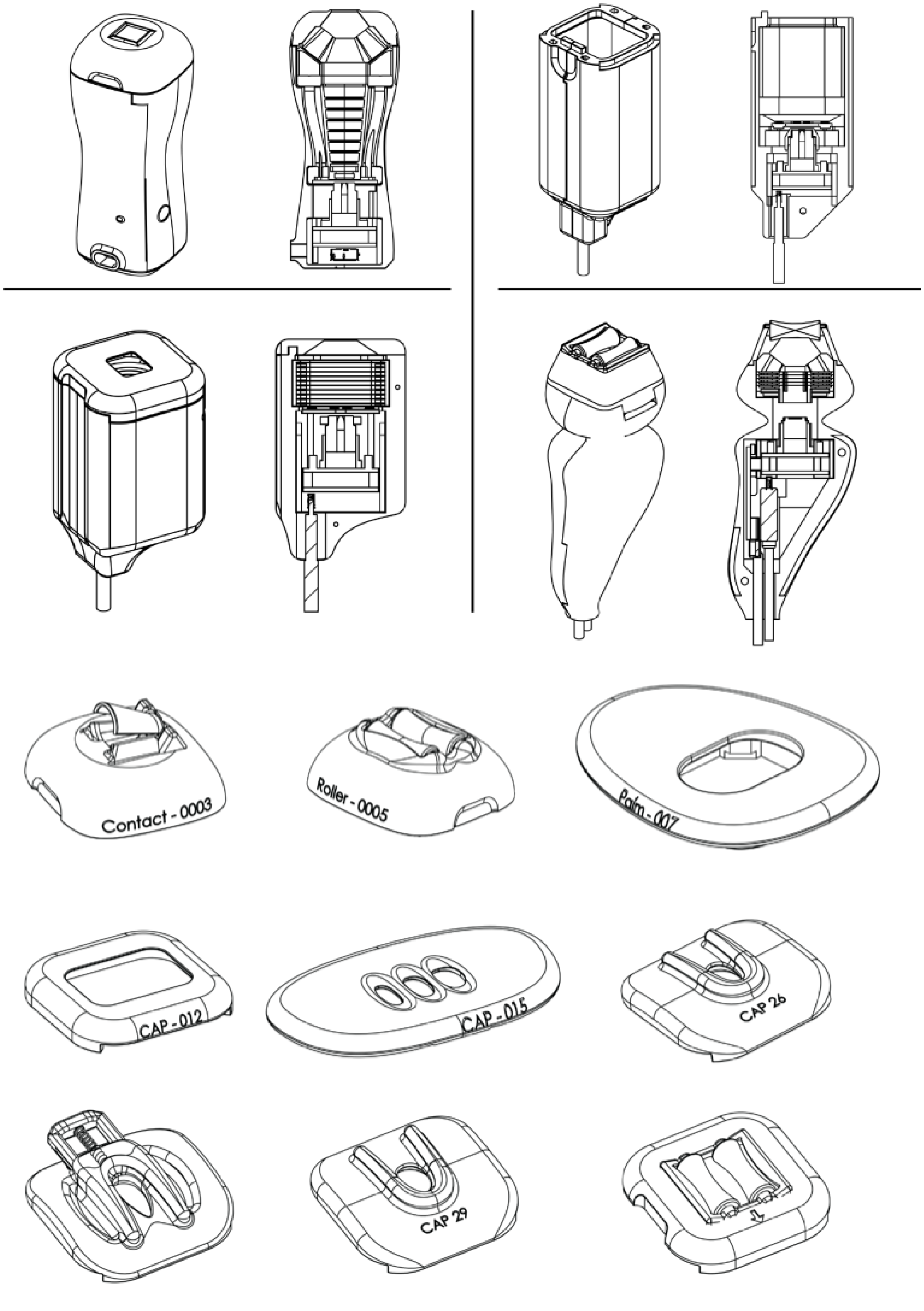

Figure D.1: Computer Aided Design (CAD) line drawing of the final hardware modules and interaction caps that fit on top of this modules.

Bibliography

[1] D. Drotman, S. Jadhav, M. Karimi, and M. T. Tolley, “3d printed soft actuators for a legged robot capable of navigating unstructured terrain *,” in *Robotics and Automation (ICRA), 2014 IEEE International Conference on*, p. in press, IEEE, 2017.

[2] D. D. P. deZonia and M. T. Tolley, “Low-cost open-source mechanical tester for soft robotics,” *2016 Robotics: Science and Systems Conference, Robot Makers: The future of digital rapid design and fabrication of robots*, 2016.

[3] S. S. Srinivasa, D. Ferguson, C. J. Helfrich, D. Berenson, A. Collet, R. Diankov, G. Gallagher, G. Hollinger, J. Kuffner, and M. V. Weghe, “HERB: A home exploring robotic butler,” *Autonomous Robots*, vol. 28, no. 1, pp. 5–20, 2010.

[4] K. Chinzei and K. Miller, “Towards MRI guided surgical manipulator,” *Medical Science Monitor*, vol. 7, no. 1, pp. 153–163, 2001.

[5] M. J. H. Lum, D. Trimble, J. Rosen, K. Fodero, H. H. King, G. Sankaranarayanan, J. Dosher, R. Leuschke, B. Martin-Anderson, M. N. Sinanan, and B. Hannaford, “Multidisciplinary Approach for Developing a New Minimally Invasive Surgical Robotic System,” *Biomedical Robotics and Biomechatronics, 2006. BioRob 2006. The First IEEE/RAS-EMBS International Conference on*, pp. 841–846, 2006.

[6] D. C. H. Yang and T. W. Lee, “Feasibility Study of a Platform Type of Robotic Manipulators from a Kinematic Viewpoint,” *Journal of Mechanical Design*, vol. 106, no. 2, pp. 191–198, 1984.

[7] O. Khatib, “Real-Time Obstacle Avoidance for Manipulators and Mobile Robots,” *The International Journal of Robotics Research*, vol. 5, no. 1, pp. 90–98, 1986.

[8] D. Rus and M. T. Tolley, “Design, fabrication and control of soft robots,” *Nature*, vol. 521, no. 7553, pp. 467–475, 2015.

[9] N. Lu and D.-H. Kim, “Flexible and stretchable electronics paving the way for soft robotics,” *Soft Robotics*, vol. 1, no. 1, pp. 53–62, 2014.

[10] R. K. Katzschmann, A. D. Marchese, and D. Rus, "Autonomous Object Manipulation Using a Soft Planar Grasping Manipulator," *Soft Robotics*, vol. 2, no. 4, pp. 155–164, 2015.

[11] M. Calisti, M. Giorelli, G. Levy, B. Mazzolai, B. Hochner, C. Laschi, and P. Dario, "An octopus-bioinspired solution to movement and manipulation for soft robots," *Bioinspiration & biomimetics*, vol. 6, no. 3, p. 036002, 2011.

[12] Y. Koseki, T. Arai, K. Sugimoto, T. Takatuji, and M. Goto, "Design and accuracy evaluation of high-speed and high precision\nparallel mechanism," *Proceedings. 1998 IEEE International Conference on Robotics and Automation (Cat. No.98CH36146)*, vol. 2, no. May, pp. 1340–1345, 1998.

[13] Y. X. Su, B. Y. Duan, C. H. Zheng, Y. F. Zhang, G. D. Chen, and J. W. Mi, "Disturbance-Rejection High-Precision Motion Control of a Stewart Platform," *IEEE Transactions on Control Systems Technology*, vol. 12, no. 3, pp. 364–374, 2004.

[14] M. T. Tolley, R. F. Shepherd, B. Mosadegh, K. C. Galloway, M. Wehner, M. Karpelson, R. J. Wood, and G. M. Whitesides, "A resilient, untethered soft robot," *Soft Robotics*, vol. 1, no. 3, pp. 213–223, 2014.

[15] D. Katz and O. Brock, "Manipulating articulated objects with interactive perception," in *2008 IEEE International Conference on Robotics and Automation*, pp. 272–277, May 2008.

[16] R. V. Martinez, J. L. Branch, C. R. Fish, L. Jin, R. F. Shepherd, R. M. D. Nunes, Z. Suo, and G. M. Whitesides, "Robotic tentacles with three-dimensional mobility based on flexible elastomers," *Advanced Materials*, vol. 25, no. 2, pp. 205–212, 2013.

[17] T. Ranzani, G. Gerboni, M. Cianchetti, and A. Menciassi, "A bioinspired soft manipulator for minimally invasive surgery," *Bioinspiration & Biomimetics*, vol. 10, no. 3, p. 35008, 2015.

[18] H. Ren, X. Gu, and K. L. Tan, "Human-compliant body-attached soft robots towards automatic cooperative ultrasound imaging," in *Computer Supported Cooperative Work in Design (CSCWD), 2016 IEEE 20th International Conference on*, pp. 653–658, IEEE, 2016.

[19] M. Manti, A. Pratesi, E. Falotico, M. Cianchetti, and C. Laschi, "Soft assistive robot for personal care of elderly people," in *2016 6th IEEE International Conference on Biomedical Robotics and Biomechatronics (BioRob)*, pp. 833–838, June 2016.

[20] A. D. Marchese, R. K. Katzschmann, and D. Rus, "A Recipe for Soft Fluidic Elastomer Robots," *Soft Robotics*, vol. 2, no. 1, pp. 7–25, 2015.

[21] S. Kim, E. Hawkes, K. Choy, M. Joldaz, J. Foleyz, and R. Wood, "Micro artificial muscle fiber using niti spring for soft robotics," in *Intelligent Robots and Systems, 2009. IROS 2009. IEEE/RSJ International Conference on*, pp. 2228–2234, IEEE, 2009.

[22] Y. Bar-Cohen, *Electroactive polymer (EAP) actuators as artificial muscles: reality, potential, and challenges*, vol. 136. SPIE press, 2004.

[23] K. Suzumori, S. Iikura, and H. Tanaka, "Applying a flexible microactuator to robotic mechanisms," *IEEE Control Systems*, vol. 12, pp. 21–27, Feb 1992.

[24] M. Luo, W. Tao, F. Chen, T. K. Khuu, S. Ozel, and C. D. Onal, "Design improvements and dynamic characterization on fluidic elastomer actuators for a soft robotic snake," in *Technologies for Practical Robot Applications (TePRA), 2014 IEEE International Conference on*, pp. 1–6, IEEE, 2014.

[25] P. Polygerinos, N. Correll, S. A. Morin, B. Mosadegh, C. D. Onal, K. Petersen, M. Cianchetti, M. T. Tolley, and R. F. Shepherd, "Soft robotics: Review of fluid-driven intrinsically soft devices; manufacturing, sensing, control, and applications in human-robot interaction," *Advanced Engineering Materials*, pp. e201700016–n/a. e201700016.

[26] R. K. Katzschmann, A. D. Marchese, and D. Rus, "Hydraulic autonomous soft robotic fish for 3d swimming," in *Experimental Robotics*, pp. 405–420, Springer, 2016.

[27] A. D. Marchese, K. Komorowski, C. D. Onal, and D. Rus, "Design and control of a soft and continuously deformable 2D robotic manipulation system," *Proceedings - IEEE International Conference on Robotics and Automation*, pp. 2189–2196, 2014.

[28] B. Mosadegh, P. Polygerinos, C. Keplinger, S. Wennstedt, R. F. Shepherd, U. Gupta, J. Shim, K. Bertoldi, C. J. Walsh, and G. M. Whitesides, "Pneumatic networks for soft robotics that actuate rapidly," *Advanced Functional Materials*, vol. 24, no. 15, pp. 2163–2170, 2014.

[29] H. Apparatus, "Phd 2000 syringe pump series user's manual," 2011.

[30] H. Lipson, "Challenges and Opportunities for Design, Simulation, and Fabrication of Soft Robots," *Soft Robotics*, vol. 1, no. 1, pp. 21–27, 2013.

[31] H. Yabu, "Fabrication of mesoscale polymer structures by self," *IEEE Spectrum*, vol. 89, p. 43, 1989.

[32] R. F. Shepherd, F. Ilievski, W. Choi, S. A. Morin, A. A. Stokes, A. D. Mazzeo, X. Chen, M. Wang, and G. M. Whitesides, "Multigait soft robot," *Proceedings of the National Academy of Sciences*, vol. 108, no. 51, pp. 20400–20403, 2011.

[33] A. Zolfagharian, A. Z. Kouzani, S. Y. Khoo, A. A. A. Moghadam, I. Gibson, and A. Kaynak, "Evolution of 3D printed soft actuators," *Sensors and Actuators, A: Physical*, vol. 250, no. October, pp. 258–272, 2016.

[34] B. N. Peele, T. J. Wallin, H. Zhao, and R. F. Shepherd, "3d printing antagonistic systems of artificial muscle using projection stereolithography," *Bioinspiration & biomimetics*, vol. 10, no. 5, p. 055003, 2015.

[35] J. Morrow, S. Hemleben, and Y. Menguc, "Directly fabricating soft robotic actuators with an open-source 3-d printer," *IEEE Robotics and Automation Letters*, vol. 2, pp. 277–281, Jan 2017.

[36] G. Udupa, P. Sreedharan, P. Sai Dinesh, and D. Kim, "Asymmetric bellow flexible pneumatic actuator for miniature robotic soft gripper," *Journal of Robotics*, vol. 2014, 2014.

[37] G. Agarwal, N. Besuchet, B. Audergon, and J. Paik, "Stretchable materials for robust soft actuators towards assistive wearable devices," *Nature Publishing Group*, vol. 6, p. 34224, 2016.

[38] D. Philippe, O.-B. Jean-Marie, G.-D. Marta, and C. Thomas, "Global immunization: status, progress, challenges and future," *BMC International Health and Human Rights*, vol. 9, no. Suppl 1, p. S2, 2009.

[39] D. Maltoni, D. Maio, A. K. Jain, and S. Prabhakar, *Handbook of Fingerprint Recognition*. Springer, 2009.

[40] A. K. Jain, A. Ross, and S. Prabhakar, "An Introduction to Biometric Recognition," vol. 14, no. 1, pp. 4–20, 2004.

[41] EyeLock LLC, "Accelerate Authentication Throughput . HBOX for business , government and consumers . NO IRIS , NO ID," 2016.

[42] M. Tartagni and R. Guerrieri, "A fingerprint sensor based on the feedback capacitive sensing scheme," *IEEE Journal of Solid-State Circuits*, vol. 33, no. 1, pp. 133–142, 1998.

[43] M. L. Sheu, W. H. Hsu, and Y. C. Huang, "Low parasitic capacitance and low-power CMOS capacitive fingerprint sensor," *Journal of Information Science and Engineering*, vol. 26, no. 2, pp. 585–595, 2010.

[44] A. Shimizu and M. Hase, "Entry method of fingerprint image using prism," *Trans. Inst. Electron. Commum. Eng. Jpn*, vol. 67, pp. 627–628, 1984.

[45] A. Rev, "Lumidigm V-Series Fingerprint Sensor Specification," no. January, pp. 1–8, 2015.

[46] R. M. Schmitt, W. G. Scott, R. D. Irving, J. Arnold, C. Bardons, D. Halpert, and L. Parker, "Ultrasonic imaging of fingerprints using acoustical impediography," in *IEEE Ultrasonics Symposium, 2004*, vol. 1, pp. 680–688 Vol.1, Aug 2004.

[47] S. S. Id and L. Pro, "Qualcomm ® Snapdragon Sense ID 3D Qualcomm ' s New Ultrasonic Fingerprint Sensor," 2016.

[48] P. J. Phillips, H. Moon, P. Rauss, and S. Rizvi, "The {FERET} evaluation methodology for face recognition algorithms," *IEEE Proceedings of Computer Vision and Pattern Recognition*, pp. 137–143, 2000.

[49] D. Zhang and W. Shu, "Two novel characteristics in palmprint verification: datum point invariance and line feature matching," *Pattern Recognition*, vol. 32, no. 4, pp. 691–702, 1999.

[50] NSTC, "Palm print recognition system," *Computer Communications*, vol. 7, no. 6, p. 325, 1984.

[51] J. Cross and C. Smith, "Thermographic imaging of the subcutaneous vascular network of the\nback of the hand for biometric identification," *Proceedings The Institute of Electrical and Electronics Engineers. 29th Annual 1995 International Carnahan Conference on Security Technology*, no. v, 1995.

[52] F. Prokoski, "History, current status, and future of infrared identification," *Proceedings IEEE Workshop on Computer Vision Beyond the Visible Spectrum: Methods and Applications (Cat. No.PR00640)*, pp. 5–14, 2000.

[53] S. Tiwari, A. Singh, and S. K. Singh, "Intelligent Method for Face Recognition of Infant," *International Journal of Computer Applications*, vol. 52, no. 4, pp. 975–8887, 2012.

[54] S. Bharadwaj, H. S. Bhatt, R. Singh, M. Vatsa, and S. K. Singh, "Face recognition for newborns: A preliminary study," *IEEE 4th International Conference on Biometrics: Theory, Applications and Systems, BTAS 2010*, pp. 3–8, 2010.

[55] D. Weingaertner, O. Bellon, L. Silva, and M. Cat, "Newborn's Biometric Identification: Can it be done?," *Visapp (1)*, pp. 200–205, 2008.

[56] C. Fields, H. C. Falls, C. P. Warren, and M. Zimberoff, "The ear of the infant as an identification constant," 1960.

[57] J. Cao, W. Shi, A. Salim, and P. Kilgore, "MyPalmVein: A Palm Vein-Based Low-Cost Mobile Identification System for Wide Age Range," *Proceedings - 2016 IEEE 1st International Conference on Connected Health: Applications, Systems and Engineering Technologies, CHASE 2016*, pp. 324–325, 2016.

[58] F. Galton., "Finger prints of young children," 1899.

[59] S. Tiwari, "Newborn ' s Ear Recognition : Can it be done ?," no. Iciip, pp. 9–14, 2011.

[60] G. Schumacher, *Fingerprint Recognition for Children.* 2013.

[61] A. K. Jain, S. S. Arora, K. Cao, L. Best-Rowden, and A. Bhatnagar, "Fingerprint Recognition of Young Children," *IEEE Transactions on Information Forensics and Security*, vol. 12, no. 7, pp. 1–1, 2016.

[62] Y. Koda, T. Higuchi, and A. K. Jain, "Advances in capturing child fingerprints: A high resolution CMOS image sensor with SLDR method," *Lecture Notes in Informatics (LNI), Proceedings - Series of the Gesellschaft fur Informatik (GI)*, vol. P-260, pp. 1–8, 2016.

[63] S. Mil'shtein and U. Doshi, "Scanning the pressure-induced distortion of fingerprints," *Scanning*, vol. 26, no. 6, pp. 270 –272, 2004.

[64] K. H. Fieldingt, J. L. Horner, and C. K. Makekau, "Optical fingerprint identification by binary joint transform correlation.," tech. rep., ROME AIR DEVELOPMENT CENTER GRIFFISS AFB NY, 1990.

[65] Y. Chen, G. Parziale, E. Diaz-Santana, and A. K. Jain, "3D touchless fingerprints: Compatibility with legacy rolled images," *Biometrics Symposium, BCC 2006*, pp. 1–6, 2006.

[66] P. Wiggin, L. Ericson, and D. Ph, "Contactless Fingerprint Technologies Assessment DOJ Office of Justice Programs National Institute of Justice," *U.S. Department of Justice*, no. Version 2, 2014.

[67] M. D. Garris, E. Tabassi, and C. L. Wilson, "NIST fingerprint evaluations and developments," *Proceedings of the IEEE*, vol. 94, no. 11, pp. 1915–1925, 2006.

[68] M. Kass and A. Witkin, "Analyzing oriented patterns," *Computer vision, graphics, and image processing*, vol. 37, no. 3, pp. 362–385, 1987.

[69] P. D. Welch, "The Use of Fast Fourier Transform for the Estimation of Power Spectra: A Method Based on Time Averaging Over Short, Modified Periodograms," *IEEE Transactions on Audio and Electroacoustics*, vol. 15, no. 2, pp. 70–73, 1967.

[70] C. Identification and I. Polymers, "Safety data sheet HydroSpan 400 Safety data sheet," 2012.